A Study of the Redshift Dependency in the Formation and Evolution of the Intra-Cluster Light

Capucine Barfety

Department of Physics

McGill University

Montréal, Québec, Canada

September 9, 2021

A thesis presented for the degree of Masters of Physics

Abstract

The formation and evolution of Brightest Cluster Galaxies (BCG) and the Intra-Cluster Light (ICL), as well as how they relate to one another, is to this day poorly understood. They most likely are the result of a complex evolutionary path, and sit at the crossroad of many processes such as galaxy interactions, cooling flows, or even Active Galactic Nuclei feedback. In this work, I probe the redshift dependency of the formation of the ICL, first through the analysis of a disrupted $z = 1.71$ starbursting cluster core; and then by investigating the light profile of $\sim$ 890 clusters of mass $\sim 2 \times 10^{14}\ M_{\odot}$ spanning $0.175 \leq z \leq 1.9$, in the hope to resolve the apparition of the intra-cluster light during this epoch. In the case of the starbursting core, I make an estimate for the stellar mass recently formed in the region, amounting to $(1.00 \pm 0.18) \times 10^{11}\ M_{\odot}$. This much mass - along with the presence of a giant molecular gas reservoir and the high star formation rate - endorses the idea that we are in fact witnessing the *in-situ* formation of the ICL. For the analysis of the cluster sample, the stacked light profiles of the clusters at redshift $0.2 < z < 0.3$, $0.5 < z < 0.6$, $0.7 < z < 0.8$, $1 < z < 1.2$, and $1.5 < z < 1.6$ are investigated after correcting for various redshift effects.

The light profiles after correcting for the passive evolution of stars are strikingly similar, indicating that the ICL might depend more strongly on the cluster mass than it does on redshift; while being composed of stellar populations formed at similar epochs.

Abrégé

La formation et l'évolution de la galaxie la plus brillante d'un amas (brightest cluster galaxy, BCG) et de la lumière intra-amas (intra-cluster light, ICL), ainsi que leur relation l'un à l'autre, sont à ce jour mal compris. Il semblerait que ces deux systèmes soient le résultat d'une évolution complexe, situés au carrefour de nombreux phénomènes tel que les interactions entre galaxies, les courants de refroidissement, voir même la rétroaction de noyau actif de galaxie. Ce mémoire se penche sur la dépendance entre le décalage spectral et la formation de l'ICL. En premier lieu, à travers l'analyse du centre d'un amas de galaxies à $z = 1.71$ formant activement des étoiles; puis à travers l'étude de la courbe de croissance de ~ 890 amas de masse $\sim 2 \times 10^{14} M_{\odot}$ entre $z = 0.175$ et $z = 1.9$, dans l'espoir d'observer l'apparition de l'ICL à cette époque. Dans le cas de l'amas à $z = 1.71$, la quantité de masse stellaire récemment formée dans la région est estimée à $(1.00 \pm 0.18) \times 10^{11}\ M_{\odot}$. Cette quantité de masse, combinée à la présence d'un réservoir géant de gaz moléculaire et à un rythme de formation d'étoiles élevé, soutient l'hypothèse que l'ICL est formé sur place dans ce cas précis. Pour ce qui est de l'analyse de l'échantillon d'amas, la courbe de croissance combinée

des amas à $0.2 < z < 0.3$, $0.5 < z < 0.6$, $0.7 < z < 0.8$, $1 < z < 1.2$, et $1.5 < z < 1.6$ sont investiguées après avoir corrigé de multiples effets liés au redshift. Après avoir fait évoluer les populations d'étoiles, les courbes sont extrèmement similaires, ce qui indique que la lumière intra-amas pourrait dépendre plus fortement sur la masse des amas que sur leur redshift; malgré que les étoiles qui la composent soit formées à des époques similaires.

Acknowledgements

First and foremost, I would like to thank Professor Tracy Webb, who not only introduced me to the world of research and astronomy; but who provided me with guidance all throughout my degree, and helped me shape and complete this project.

I would also like to thank Professor Adam Muzzin, for his invaluable input and the time he has spent helping me understand some of the methods used in this project over the last few months.

Thank you to my friends for their countless words of encouragement, and in particular to my fellow physics graduate student, Alaina Giang Bui, who supported me in my research, and made the isolation tolerable in times of a global pandemic.

Finally, I would like to thank my family, especially my parents, for providing me with their unwavering support, despite being on different continent.

Contents

List of Figures

List of Tables

List of Acronyms

AGN	Active Galactic Nuclei.
BCG	Brightest Cluster Galaxy.
CCD	Charge-Coupled Device.
CG	Central Galaxy.
DES	Dark Energy Survey.
DSC	Diffuse Stellar Component.
HST	Hubble Space Telescope.
ICL	Intra-Cluster Light.
ICM	Intra-Cluster Medium.
IHL	Intra-Halo Light.
IMF	Initial Mass Function.
IR	Infrared.
ISM	Inter-Stellar Medium.
IVM	Inverse-Variance Map.

LMT	Large Millimeter Telescope.
NCSA	National Center for Supercomputing Applications.
NIR	Near-Infrared.
PCA	Principle Component Analysis.
PSF	Point Spread Function.
SAM	Semi-Analytic Model.
SDSS	Sloan Digital Sky Survey.
SED	Spectral Energy Distribution.
SF	Star Formation.
SFR	Star Formation Rate.
SMBH	SuperMassive Black Hole.
SpARCS	Spitzer Adaptation of the Red-sequence Cluster Survey.
VLA	Very Large Array.
WFC3	Wide Field Camera 3.

Chapter 1

Introduction

As the largest bound structures in the known Universe, galaxy clusters are ensembles of gravitationally bound galaxies, at the center of which often lies one particular massive and bright galaxy, named the Brightest Cluster Galaxy (BCG). BCGs are generally giant ellipticals, some of which identified as cD, with an extended envelop of diffuse light (Oemler 1973 [12]). However, it has since been discovered that some of this extended halo is in fact a separate component of the cluster, named the Intra-Cluster Light (ICL).

First proposed by Zwicky 1937 [13], and later observed for the very first time in the Coma cluster (Zwicky 1951 [14]), the existence of the ICL was theorized to solve the missing baryon problem. While it quickly became obvious that the ICL cannot amount for all of the missing mass, its discovery shone light on a new component of galaxy clusters. It was then conjectured that this halo is linked to BCGs (Oemler 1976 [15]) and their formation history,

however observations of clusters with an extended halo of light but without a central galaxy (Vílchez-Gómez et al. 1994 [16]) established the idea that the ICL is a component tied to the evolution of the cluster itself, rather than the BCG. Nowadays, the ICL refers to a halo of diffuse light, composed of unbound stars, and seemingly concentrated around the cluster potential. It is thought to be a direct result of the clusters' dynamics, and therefore is key to the understanding the evolution process of clusters. The formation and evolution of the intra-cluster has thus been extensively studied ever since.

Indeed, in the past 50 years, there has been monumental progress in the study of the ICL. On one hand, the advent of CCDs allowed for much deeper observations of the ICL (eg: DeMaio et al. 2018 [17], 2020 [18]; Burke et al. 2015 [2]), with both better resolution and at higher redshifts (Ko & Jee 2018 [19], Burke et al. 2012 [20]). On the other hands, SAMs (eg: Contini et al. 2014, 2018 [5, 21]) and hydro-dynamical simulations (eg: Puchwein et al. 2010 [22], Rudick et al. 2011 [1]) have become more complex, and can now reproduce the observed ICL, providing great insight on the formation and evolution of this component. As of today, the ICL is thought to represent $\sim 10 - 20\%$ of the total stellar mass of the cluster (eg: Puchwein et al. 2010 [22], Contini et al. 2018 [21], Ko & Jee 2018 [19]).

However, studying the ICL is a delicate task. It is at most 1% of the brightness of the sky, and the distinction between the clusters galaxies and the ICL is to this day not well established. Moreover, observational constraints put a damper on the quality of the detection: the size of the Point Spread Function (PSF), as well as the sky subtraction

process, have be shown to influence the measurements of the intra-cluster light (Tang et al. 2018 [6], Furnell et al. 2021 [4]). In addition, the measured ICL is highly dependent on the definition used to identify it, making matters more complicated (Tang et al. 2018 [6]). Among others, the epoch of formation of the ICL, as well as its redshift evolution, is still poorly defined, despite numerous studies on the subject.

This work studies said redshift evolution of the ICL, through the detailed analysis of SpARCS clusters, using: 1) the analysis of the stellar mass in the Intra-Cluster Medium (ICM) of a $z = 1.71$ cluster, using the photometric M/L conversions from Bell et al. 2003 [23]; and 2) the study of the light profile out to 500 kpc of a large (> 800) sample of clusters between $0.175 < z < 1.9$, to detect the presence of the ICL over this redshift range through the stacking of clusters in three redshift bins deemed significant in the ICL history.

The organisation of this thesis is as follow: Chapter 2 presents an overview of the ICL in the literature, both in terms of the properties of the ICL and its current theories on its formation. Then, Chapter 3 presents the analysis of the disrupted $z = 171$ cluster, SpARCSJ104922.6+564032.5, which might indicate *in-situ* formation of the ICL. Chapter 4 covers the second part of the thesis, which focuses on the SpARCS clusters' light profiles. Finally, Chapter 5 discusses the results and implication of the two previous chapters, and compares said results to previous studies; and Chapter 6 concludes the thesis.

Chapter 2

The ICL in the Literature

As the ICL was identified as a ubiquitous feature of galaxy clusters, tightly linked to the assembly history of the associated cluster, it became increasingly important to understand how it forms. Its shape, age, color, give us invaluable information on the governing processes a play, and allow to discriminate between mechanisms. Understanding the intrinsic properties of the ICL has been the focus of many studies, and the most up-to-date conclusions are presented here.

The organisation is as follow: §2.1 reviews the current definitions and known properties of the ICl, as well as the challenges faced by astronomers. Then, §2.2 explores the current theories on BCG and ICL formation and evolution - through both the eyes of simulations and observations. The section was written exclusively by C. Barfety.

2.1 Properties of the ICL

The ICL is generally defined as the halo of light ubiquitous to galaxy clusters, constituted of stars, not bound to any of the cluster galaxies, but rather to the potential of the cluster (Montes et al. 2019 [24]). Studying it is a challenge, as the ICL is as its brightest only 1% of the sky's brightness. Nonetheless, since its discovery, the scientific community has been working on identifying its distinctive features and properties - light profile, metallicity, age - which might vary as a function of the cluster mass, or the redshift of the host cluster for example. This section goes over the results of past studies, and the challenges in studying the ICL. It should be noted that while the examples cited below are in no way an exhaustive list of the studies on the ICL; they clearly demonstrate the contradicting results on the intrinsic properties of this component.

2.1.1 Defining the ICL

There are two main methods used to define the ICL: 1) the surface brightness (SB) limit method, and 2) the SB profile method. The first one is rather straightforward, and consists in setting a SB threshold, where all the measured flux below that limit is considered as ICL. However, the chosen limit in itself is fairly different depending on the study: Burke et al. 2015 [2] and Furnell et al 2021. [4] use a surface brightness limit of $\mu_B = 25$ mag/arcsec^2 in the rest-frame B-band, Ko & Jee 2019 [19] use $\mu_B = 25$ mag/arcsec^2 and $\mu_R = 26$ mag/arcsec^2 in the rest-frame B and R band respectively, or even Feldmeier et al. 2004 [25]

uses $\mu_V = 26.5$ mag/arcsec^2 in the V band, to cite only a few. This is a problem because, as shown by Tang et al. 2018 [6], the ICL fraction is strongly dependant on this limit: if the limit is too high, then it will engulf flux from the galaxies; and if the limit is too low then the ICL for a given cluster is underestimated. The other method on the other hand relies on separating the ICL from the galaxies by examining its intrinsic properties, such as its surface brightness profile (eg: Gonzalez et al. 2007 [26], Zhang et al. 2019 [11]) or mass distribution (eg: DeMaio et al. 2015 [27]). A large amount of studies using this second method also do not attempt to separate the BCG and ICL, and often consider the BCG+ICL light profile, since the frontier between the two is not well defined (eg: Gonzalez et al. 2007 [26], DeMaio et al. 2020 [18]).

It should be noted that many studies quote their measured ICL in the form of the ICL fraction, i.e., the fraction of total cluster light (or stellar mass) the ICL represents. Throughout the literature, there is an overall tension between the results in ICL fraction from simulations (in particular hydrodynamical simulations) and the ones derived from observations. This tension is partly shown Figure 2.1, where the results from simulations are generally higher than those based on observations. In the most extreme cases, the ICL fraction from simulations can reach $\sim$ 45% (Puchwein et al. 2010 [22]). One possible explanation for this systematic is the difference in ICL definitions which leads to either an overestimation of the ICL in simulations or an underestimation in observations, if not both. For this reason, studies on the tension between simulations and observations have insisted

on the importance of using similar definitions when studying the ICL (eg: Tang et al. 2018 [6]).

2.1.2 Redshift Evolution of the ICL

The evolution of the ICL with redshift is a longstanding question. Simulations generally agree that the bulk of the ICL forms below $z \sim 1$: Contini et al. 2018 [21] finds an increase in stellar mass fraction from $< 5\%$ at $z = 1$ to $\sim 12\%$ at $z = 0$. Rudick et al. 2006 [28] finds an increase in the ICL fraction from $\sim 3\%$ at redshift 2 to $\sim 15\%$ at redshift 0, and Murante et al. 2007 finds that $\sim 75\%$ of the Diffuse Stellar Component (DSC) forms after $z = 1$.

Observationally, the results are less conclusive. Burke et al. 2015 studies 25 clusters between $0.18 < z < 0.9$, and finds that the ICL increase by 4-5 in the range $0.18 < z < 0.4$ (imaging of higher redshift clusters is not deep enough to measure the ICL, so they are discarded). The range is displayed in green in the left panel of Figure 2.1. Similarly, Furnell et al. 2021 [4] caries the analysis of 18 clusters between $0.1 < z < 0.8$, and observe a growth factor of 2-4 between $0.1 < z < 0.5$. The results between the two studies are very similar, which may partly be because they use similar ICL definitions, over a similar redshift range. On the other hand, Morishita et al. 2017 [29] and Montes & Trujillo 2018 [3] find by examining the same 6 clusters from the Hubble Frontier Fields between $0.3 < z < 0.6$ that there is no particular trend of ICL fraction with redshift; although the authors state that this might be a result of spanning a narrow redshift range with a small sample. The ICL fractions

as a function of redshift computed by Montes & Trujillo 2018 [3] are displayed on the left panel of Figure 2.1, using three different prescriptions to define the ICL. All three result in different ICL fractions, but none of them show any trend with decreasing redshift. Supporting the results from the Frontier Field clusters, Jiménez-Teja et al. 2018 [30] finds no significant increase in ICL fraction with redshift when studying 11 clusters between $0.187 < z < 0.548$.

Finally, the detection of the ICL in a $z = 1.24$ cluster by Ko & Jee 2018 [19] opens a new window of possibilities. The analysis of the HST data reveals an ICL component representing at least $\sim 10\%$ of the total cluster light. Not only is this the highest redshift detection of the ICL; but the fact that it represents a sizable fraction of the total cluster light contradicts most theoretical and observational studies to this day.

2.1.3 The ICL as a Function of Cluster Mass

Similar to the redshift evolution of the ICL, the dependence of the ICL fraction on the cluster mass is poorly understood. The analysis carried by Furnell et al. 2021 finds that the ICL represents around 24% of the total cluster stellar mass, and that this fraction is not dependant on cluster mass, as shown in in the right panel of Figure 2.1. These results are once again in agreement with those from Burke et al. 2015 [2], which also show no trend with cluster mass (black circles on the right panel of Figure 2.1). Contradicting these studies, DeMaio et al. 2018 [17] reports a growth of the ICL component with cluster mass, as the stellar mass in the inner 100kpc of the cluster sample increases much faster ($\propto M_{500,c}^{0.37\pm0.05}$,

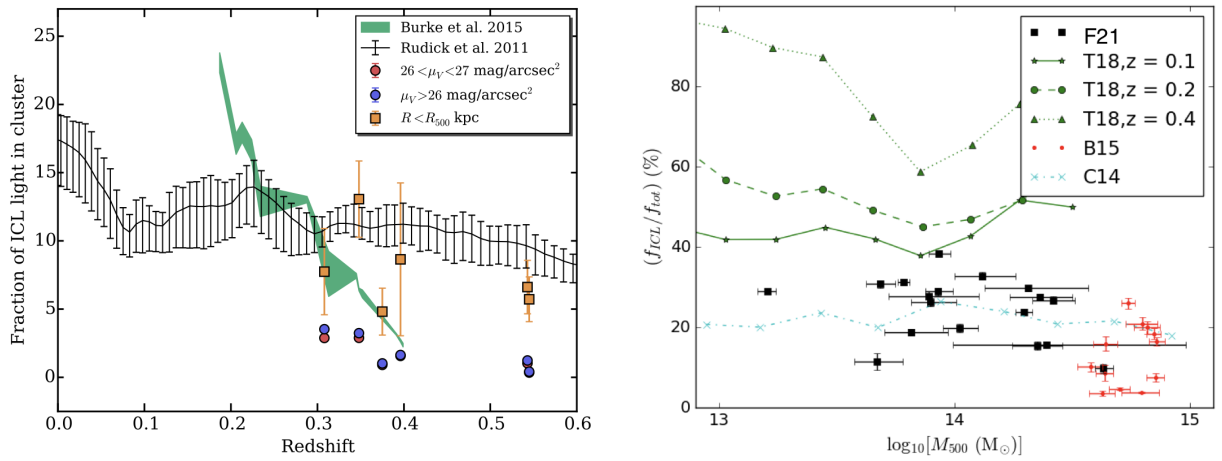

Figure 2.1: Left panel: Comparison of the predicted ICL fraction as function of redshift from simulations (Rudick et al. 2011 [1]) with the measured values from observations (Burke et al. 2015 [2], Montes and Trujillo 2018 [3]). All ICL fractions were computed using the SB limit method: $\mu_B = 25$ mag/arcsec^2 for Burke et al. 2015, $\mu_V = 26$ mag/arcsec^2 for Rudick et al. 2011 and Montes & Trujillo 2018. Figure adapted from Montes and Trujillo 2018 [3]. Right panel: Comparison of the ICL fraction as a function of halo mass from simulations and observations. F21 refers to the results from Furnell et al. 2021 [4], B15 refers to Burke et al. 2015 [2], C14 refers to the results from from Contini et al. 2014 [5]'s tidal disruption model, and T18 refers to the simulations from Tang et al. 2018 [6], for three different redshifts. Figure adapted from Furnell et al. 2021 [4]. Both panels clearly show the discrepancies in ICL fraction - as well as its dependence on redshift and cluster mass - between theoretical and observational studies.

where $M_{500,c}$ is the mass of the cluster inside the radius where the cluster overdensity is 500 higher than the critical density of the Universe) with cluster mass than the mass in the inner 10kpc ($\propto M_{500,c}^{0.17\pm0.06}$). Similarly, both Zhang et al. 2019 [11] and Sampaio-Santos et al. 2021 [31] show by stacking clusters from the Dark Energy Survey (DES) at $0.2 < z < 0.35$ that there is a clear dependence between the amount of ICL outside the cluster center and the mass of the cluster.

Likewise, simulation results are contradictory: some (eg: Puchwein et al. 2010 [22], Contini et al. 2014 [5], in the right panel of Figure 2.1) report no trend with halo mass, whereas others (eg: Murante et al. 2007 [32], Purcell et al. 2007 [33]) report an increasing ICL fraction with cluster mass. Finally, in opposition with all the above, Cui et al. 2014 [34] find a decreasing ICL fraction with increasing cluster mass. The contradictions do not seem to arise from the differences between SAMs and hydrodynamical models either.

2.1.4 The Stellar Populations of the ICL

Finally, the study of the stellar populations which constitute the ICL, to determine their age, colour, or metallicity, has attracted a lot of attention. Indeed, since the observed properties of the stellar populations of the ICL are dependent their origins, they can therefore help identify the process through which the intra-cluster light formed, as well as give valuable insight on the history of the cluster itself.

Research by Morishita et al. 2017 [29], mentioned in §2.1.2 & 2.1.3, finds that the ICL

stars are around $\sim 1-3$ Gyr old. Their observations show a strong color gradient, where the light at $r > 150$kpc from the Central Galaxy (CG) is much bluer than inside that radius, indicating the presence of a significant amount of stars with age ~ 1 Gyr in the outskirts of the ICL. Using the same clusters, but a different analysis, Montes & Trujillo 2018 [3] find the ICL stars to be between $2-6$ Gyr younger than the BCGs'. Following a similar correlation, but with conflicting numbers, Cui et al. 2014 [34] find the ICL to be $\sim 0.5-1$ Gyr younger than the BCG in average. They argue that this trend shows that the BCG and the ICL undergo two separate evolutionary processes, which is in line with most observations. The authors also observe a decreasing trend of the ICL's age with cluster mass.

Observing similar colour gradients in their sample of 23 clusters, DeMaio et al. 2018 [17] surmise that the negative colour gradient is coherent with an ICL growth linked to tidal stripping of massive quiescent galaxies, or the shredding of dwarf galaxies.

Two studies that stand out by their results on the age and color of the ICL are the following. Jiménez-Teja et al. 2018 [30] report an excess of younger stars in the ICL of merging clusters, compared to that of quiescent clusters, which could indicate that the age - and formation - of the ICL is more linked to the dynamical state of clusters than to their redshifts. On the other hand, Ko & Jee 2019 [19] observes an ICL similar in color to that of satellite galaxies, with no colour gradient. They evaluate the formation epoch of the intra-cluster stars to be roughly $z \sim 2-3$. They conclude that in this case, the growth of the ICL is more tightly linked to the growth of the BCG than current theories presuppose.

Of course, the possibility exits that this cluster is an exception, and not the rule, which is why there is a dire need for deeper resolution imaging of large numbers of $z > 1$ clusters, to investigate the ICL at higher redshifts.

2.2 The Formation of the ICL

There are five channels of formation for the ICL that have been suggested by the community. Those five channels are all expected to result in a similar light halo in clusters, but with varying properties: the amount of cluster light present, the age of the stellar population, this morphology and extent of the halo, etc,... which give a wealth of criterion to investigate in order to discriminate between the different scenarios.

2.2.1 *In-situ* Star Formation

In this scenario, part - or most - of the ICL is formed through bursts of star formation in the intra-cluster medium, unbound to any cluster galaxy. This hypothesis first came to light through simulations, in Schulz & Struck 2001 [35] and Vollmer et al. 2001 [36]. In these simulations, cooling of gas filaments stripped from galaxies in clusters can lead to the formation of stars in the halo rather than in galaxies. Later on, the presence of intra-cluster star formation was observed by Sun et al 2010 [37], through Chandra observations of Abell 3627, a rich cluster in the local Universe. In this situation, the authors conclude that ram stripping of the ISM by the ICM leads to the formation of stars in the halo of the cluster,

which might form part of the ICL (between ~ 1 and 10%).

Following these observations, *in-situ* formation of the ICL was also observed by Puchwein et al. 2010 [22]. The article presents the results from a hydro-dynamical simulation, exploring the redshift evolution of galaxy clusters, especially the distribution of the clusters' baryonic mass between the cluster galaxies, the BCG and the ICL. The simulation was novel, compared to previous work (eg: Murante et al. 2007 [32]), in that it takes into account SMBH growth and AGN feedback, where the latter is thought to be one of the main mechanisms preventing over-cooling (and over-star formation) in clusters (McNamara & Nulsen 2012 [38]). In the study, Puchwein et al. 2010 [22] find that whereas most of the intracluster stars come from the tidal disruption of infalling satellite galaxies (see §2.2.5), a non-negligible amount of stellar mass (up to 30%) is formed via *in-situ* SF, inside giant clouds of cold gas that are stripped from the galaxies during mergers and interactions.

Since then, there has been little evidence for *in-situ* SF in the ICL. A few studies reported star formation in the ICM from material stripped via ram pressure (eg: Smith et al. 2010 [39], Gullieuszik et al. 2020 [40]), but even in these cases, the fraction of the ICL formed *in-situ* is negligible: Gullieuszik et al. 2020 [40] finds that $\sim 4 \times 10^9\, M_\odot$ of stars form between $z = 1$ and $z = 0$, at a rate of $\sim 0.44\, M_\odot/yr$. Moreover, in a study by Melnick et al. 2012 [41], the analysis of the stacked X-ray spectra of a cluster at $z = 0.29$ reveals that only $\sim 8\%$ of the stars in the ICL were formed recently, seemingly disproving Puchwein's argument. It should also be noted that the tension between the light fraction in observations and Puchwein et al.

2010 [22] can be resolved if the stars formed *in-situ* are the result of a numerical error. Since then, simulations generally include the formation of the ICL as coming from tidal interaction (eg: Contini et al. 2018 [21]), where *in-situ* SF is not even considered.

2.2.2 Dwarf Galaxy Shredding

This channel of formation for the ICL is fairly straightforward. In the hierarchical formation scenario, where larger systems grow through the accretion of smaller systems; dwarf galaxies get shredded in the accretion process, and part - or all of - their stars end up feeding the intra-cluster light.

The main results in favor of this formation scenario are from Purcell et al. 2007 [33]. This study presented the results from a simulation using an analytic model, studying the growth of the Intra-Halo Light (IHL, the diffuse stellar component in both galaxy halos and cluster halos) from galaxy disruption, as a function of the system's size. The results are as follow: for a host system mass of $\leq 10^{12}\ M_{\odot}$, the IHL mass is almost entirely a result of the dissolution of galaxies with mass $\leq 10^{9}\ M_{\odot}$. As the host system's size increases (and reaches the stellar mass sizes of galaxy groups and clusters), the fraction of diffuse light coming from low-mass galaxies decreases, but still represents a significant amount; and only for masses reaching $\sim 10^{15} M_{\odot}$ does the contribution from dwarf galaxies appears to be negligible (Figure 7, Purcell et al. 2007 [33]).

The same year, two different studies based on simulations noted the growth of the ICL

through the shredding of dwarf galaxies. The first one, by Murante et al. 2007 [32], observed stellar mass growth of the Diffuse Stellar Component (DSC) via tidal dissolution of low-density galaxies. However, since the amount DSC formed this way appears to be highly dependant on the simulation's resolution, the authors note that the true contribution cannot be estimated with their results alone, and is likely overestimated. The second study, by Conroy et al. 2007 [42], uses a SAM to investigate the redshift evolution of the ICL and BCG stellar mass growth after $z = 1$. They observe that the $z = 0$ results that best fit the observational data are models where half or all of the stars from completely disrupted systems are deposited in the ICL, and intuit that the "true" model lies somewhere in-between. It should be noted that these studies support this formation channel as it relies on the complete disruption of satellite galaxies; however the authors note that their results seem to be driven by higher mass systems as opposed to lower mass ones. This disruption of high mass systems through merger events as the source of the ICL is covered in §2.2.4.

Despite those three simulations, there has been no reported observational evidence for this formation mechanism. On the contrary, observations of four clusters between $0.44 < z < 0.57$ by DeMaio et al. 2015 [27] strongly imply that the ICL cannot originate from dwarf galaxies. Indeed, in all four clusters, the ICL is reported to have a red color, as well as high metallicities, which is the opposite of what one would expect from dwarf halos. Moreover, the authors report ICL luminosities between $4 - 8\ L*$ within $10 < r < 110$ kpc from the core. The amount of dwarf galaxies required to produce these kind of luminosities is much greater

than that assessed by previous studies (Mancone et al. 2012 [43]). These evidences strongly argue against the shredding of dwarf galaxies as a main formation channel of the ICL, and no new observations have contradicted this ever since.

2.2.3 Pre-processing and Group Accretion

Another scenario brought up by multiple studies is the idea that a non-negligible amount of the ICL builds up through "pre-processing" and the accretion of small clusters. When presenting this as a main formation channel of the ICL; Mihos et al. 2004 [44] argues that the environment in smaller clusters is favorable to more galaxy interactions that will successfully tidally strip stars from halos, and build-up the ICL; before the cluster merges with another one. They show, through simulations of a Coma-like cluster, that tidal stripping through galaxy interactions results in tidal debris that are extended and no longer bound to the galaxy's potential, where 20% of the tidally disrupted stars end up ejected to at least 50 kpc from the galaxy. This idea is supported by the observations of A1914, a Bautz-Morgan type III cluster (i.e. a cluster without any remarkable cluster member), by Feldmeier et al. 2004 [25]. The cluster displays distinct tidal-like features in the ICL, a system that has been identified as a post cluster merger.

Now, the issue with this formation channel is that there are very few ways to discriminate between tidal features due to group accretion and tidal features from cluster potential and galaxy interactions. One option is to compare the dynamical state of the cluster with the

morphology of the ICL. Since in the ICM the tidal features will quickly be smoothed over, distinct tidal arcs in dynamically old clusters indicate that the source of the stripping is most likely not group accretion; and vice-versa.

In line with those studies, the N-body simulation of three clusters by Rudick et al. 2006 [28] observes the formation the ICL in discrete increments, coincident with group accretion events. The author argues that the ICL could be a valuable tracer of a cluster's dynamical history, depending on the morphology.

2.2.4 Violent Relaxation During Merger Events

Another formation scenario suggested by scientists is violent relaxation during a merger event, in which a significant portion of the galaxies' stars are stripped and end up feeding the ICL. This formation channel would likely result in a uniform colour profile, as it disrupts any pre-existing colour gradient in the galaxies.

This process is supported mainly by simulations, in which the ICL get created via major mergers. Murante et al. 2007 [32] observes that the majority of the DSC is liberated through mergers with the central galaxy (although there is non-negligible contribution from shredded low mass satellites, see §2.2.2). Similarly, the MERGER model in Contini et al. 2018 [21], which considers merger event as the sole origin of the ICL, manages to faithfully reproduce the ICL, albeit with a different mass distribution as their other model.

Now, there is a lot of evidence pointing towards the idea that violent relaxation is not

the only mechanism at play in ICL formation. In Contini et al. 2018 [21], the second model, which takes into account both tidal stripping and mergers, predicts they are only responsible for $\sim 15\%$ of the ICL build up. Moreover, in their study of 23 clusters between $0.29 < z < 0.89$, DeMaio et al. 2018 [17] observes a colour gradient in the intra-cluster light which gets bluer with increasing radius. These results are in agreement with their previous findings (DeMaio et al. 2015 [27]), and imply that violent relaxation cannot be the dominant formation mechanism of the ICL. All in all, the current favored theory for the formation of the ICL is a combination of tidal stripping of massive galaxies (see §2.2.5), which dominates the evolution, and violent relaxation from mergers, contributing on a smaller scale.

2.2.5 Tidal Stripping

As of today, the formation scenario that is considered as prevalent is the formation of the ICL through tidal stripping of satellite galaxies by either galaxy interactions or the cluster's tidal field. In this situation, compared to §2.2.3, the presence of tidal features is less correlated to the cluster's dynamical state.

Sitting at the crossroad of this scenario and the scenario described in §2.2.3, an N-body simulation by Rudick et al. 2009 [45], which focuses on following the evolution of individual cluster galaxies and their streams, finds that $\sim 40\%$ of the ICL is produced during discrete accretion events, during which galaxy mergers and interactions strip a considerable amount mass which feed the ICL. The simulation also shows that most of the ICL formed through

this process is formed early in the cluster's history, and quiets down as the cluster grows older and more massive (as galaxy interactions are rarer and massive elliptical galaxies are harder to disrupt).

On the other hand, SAMs by Contini et al. 2014 [5] and 2018 [21] have found that most of the ICL is formed via stripping of masive satellite galaxies, below $z = 1$. Both studies examine the role of tidal stripping and violent relaxation after mergers (§2.2.4), and find that the contribution of the former dominate over that of the latter. In Contini et al. 2014 [5], $> 70\%$ of the ICL is formed through stripping of galaxies with mass $> 10^{10}\, M_{\odot}$, due to their proximity with the center of the cluster where tidal forces are stronger. In Contini et al. 2018 [21], the results indicate that $\sim 90\%$ of the ICL build-up from tidal stripping occurs in the inner 150kpc of the cluster. In their model taking into account both tidal stripping and merger events, they find that 85% of the ICL is built from tidal stripping, and that most of this mass comes from smaller stripping events, as opposed to large disruptions of the galaxies.

In line with the findings from Contini et al. 2014, 2018 [5, 21], a few observations of the ICL favor the tidal stripping of large satellite galaxies as the main formation channel. Burke et al. 2015 [2] finds by observing a sample of 25 clusters between $0.1 < z < 0.9$ that the ICL grows most likely via stripping and minor merging of galaxies falling into the cluster core from the outskirts of the cluster. Similarly, a number of observational studies (DeMaio et al. 2015, 2018 [17, 27], Montes & Trujillo 2018 [3] to cite a few) argue that the reported

metallicities, color gradients, and luminosities are coherent with that of stripped medium from Milky-Way like galaxies.

Therefore, while there are still discrepancies between observations and simulations, as observed in §2.1, a lot of observational studies seem to point toward tidal stripping of massive objects as the main formation channel of the ICL.

Chapter 3

In-Situ Formation of the ICL in a z=1.71 cluster core

This chapter presents the study of the stellar mass in the vicinity of a BCG, in SpARCSJ104922.6+564032.5. This cluster presents a highly disturbed morphology, with an optically bright clumpy tidal tail which is spatially coincident with a molecular gas reservoir, a high star formation rate, and the peak of X-ray emission. All these factors indicate that this could be a detection of the formation of the cluster's ICL through star formation. After careful masking of the region, it becomes possible to retrieve the amount of stellar mass already formed in the region, and study its implications for the cluster. The analysis in the section was realized by C. Barfety, except for the masking of the region which was done by Dr. H. Shipley, at the time a post-doctoral fellow working with Dr. T.

Webb. The section was written exclusively by C. Barfety.

3.1 SpARCSJ104922.6+564032.5

3.1.1 Discovery

SpARCSJ104922.6+564032.5 (hereafter SpARCSJ1049) is a cluster at redshift $z = 1.71$, part of the Spitzer Adaptation of the Red-Sequence Cluster Survey (SpARCS), a galaxy cluster survey targeting clusters between $0 < z < 2$ (Wilson et al. 2009 [46], Muzzin et al. 2009 [47], Demarco et al. 2010 [48]), described in more detail in §4.1.1. SpARCSJ1049 was part of a study by Webb et al. 2015a [49], investigating high star formation rates in galaxy clusters at high redshifts. This cluster in particular attracted attention, as it presents with an exceptionally disturbed morphology, shown in Figures 3.1 and 3.2, with what looks like a clumpy tidal tail, seen in other major mergers. A follow-up detailed investigation revealed an AGN-corrected SFR of $860 \pm 150\ M_{\odot}$, offset from the central galaxy (marked by a red cross in Figure 3.2) by at least $\sim$ 25kpc (Webb et al. 2015b [7]).

Following its discovery, an impressive wealth of data on the cluster was obtained, with the goal to shine light on the origin of the morphology and SFR. Most of this data are displayed in Figure 3.1. While the study by Webb et al. 2015a [49] revealed many other BCGs with similar star formation rates, SpARCSJ1049 is the one presenting the most obvious disruption, and hence the best chance at figuring what might be triggering the burst of SF. It

then appeared imperative to follow-up in as many wavelengths as possible to piece together the story of this object.

As of today, the observations - and the conclusions drawn from it - are the following: HST infrared imaging (Cycle 22) determined the BCG's luminosity and mass (Webb et al. 2015b [7], displayed as a false colour image in the right panel of Figure 3.1); while the cluster mass and mass distribution were measured from weak lensing (Finner et al. 2020 [8], white contours in the right panel of Figure 3.1). MIPS-24μm emission was used to compute the SFR (Webb et al. 2015b [7], white contours in the left panel of Figure 3.1); and LMT & VLA radio imaging identified a massive molecular gas reservoir ($\sim 10^{11}\ M_{\odot}$) in the vicinity of the BCG (Webb et al. 2017 [50], Barfety et al. in prep, red contours in the left panel of Figure 3.1). Finally, the final piece of the puzzle seem to have been brought by Chandra X-ray observations, which strongly indicate the presence of a cooling flow (Hlavacek-Larrondo et al. 2020 [9], cyan contours in both panels of Figure 3.1). This study has shown that the SMBH in the BCG is devoid of any activity and that, in the absence of feedback to reheat the region, the intra-cluster gas in the cluster can cool through X-ray emission, triggering a burst of star formation.

All of this also showed another interesting feature of the system, which is that the BCG is not aligned with the peak of the X-Ray and radio emission, nor the lensing centroid, indicating that it might have been knocked off from the core of the cluster by a previous interaction, such as a merger with another cluster member. The fact that the SFR and

the CO reservoir are not spatially coincident with the BCG is what motivated the following study, to explore the mass being formed outside of any cluster galaxy, and might be forming the ICL.

3.1.2 HST Imaging and Data Reduction

For the purpose of the science goals in this chapter, the particular set of observations that are of interest are the deep HST images, from WFC3's IR channel in 2014 and 2015 (PIs: Perlmutter & Webb).

The object was targeted through both the F160W and the F105W filters, which have peak sensibility at 15369 Å and 10552 Å respectively. Converting the filters' pivot wavelengths to account for reshift, the light in the F160W image was emitted at $\lambda_{e,F160W} = 5692$ Å, whereas the light from the F105W image was emitted at $\lambda_{e,F105W} = 3908$ Å.

The resulting 28 images from F105W and 26 from F160W were drizzled into two separate files for each filter, with 0.06" pixel scale, using the STScI software to combine HST images, AstroDrizzle [1]. The F160W image has a total integration time of 9237s, whereas the F105W image has 8543s.

This study in particular focuses on a $12.9'' \times 11.7''$ cutout, centered around the tidal tail, as shown in Figure 3.2. To limit the contamination of the intra-cluster medium to the maximum, all the brights sources surrounding the tail (including the central galaxy and other

[1] http://www.stsci.edu/scientific-community/software/drizzlepac.html

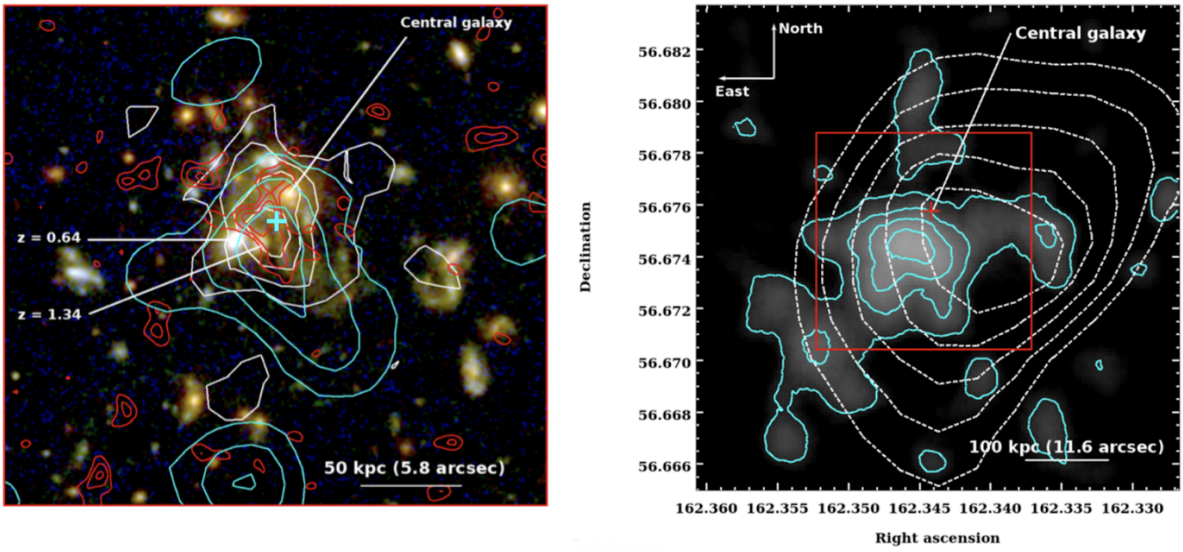

Figure 3.1: The left panel is a false-colour image of SpARCSJ+104956 using HST's F160W, F105W and F814W imaging. The red contours are the VLA data resolving the CO reservoir in the centre of the cluster (Barfety et al. in prep), while the cyan contours display Chandra's X-Ray in the 0.5 to 1 keV band. The white contours highlights the MIPS 24μm emission (Webb et al. 2015b [7]), which is centred on the tidal tail of the system. The right panel shows the contours of the Chandra X-Ray data in the 0.5 to 7 keV band (cyan) as well as the contours of the mass distribution from weak lensing (white, Finner et al. 2020 [8]). The red cross indicates the central galaxy. Both panels display the wealth of data on SpARCSJ1049, as well as the offset between the peaks of the MIPS, VLA and Chandra emission compared to the central galaxy. Figure adapted from Hlavacek-Larrondo et al. 2020 [9].

foregrounds galaxies) are fit and removed using the method from Shipley et al. 2018 [51]. The remaining traces of the galaxies' centers are manually masked before further analysis.

3.2 Methods

3.2.1 Estimating the Stellar Mass

The estimation of the stellar mass is made by multiplying the mass-to-light ratio (M/L) pixel map by the luminosity pixel map of the region, to get a pixel-by-pixel stellar mass estimate; which is then summed to obtain a total stellar mass. The steps required to make this measurement are described as follow.

The observations from HST come in units of electron per second. To obtain the magnitude from these files, we convert to units of flux density ($erg/cm^2/s/\text{Å}$) using PHOTFLAM, the inverse sensitivity parameter as given by STScI[2]. Once the conversion is done, the pixel-by-pixel ST magnitude can be retrieved using:

$$\text{STmag} = -2.5\log_{10}(F_\lambda) - 21.10 \tag{3.1}$$

where F_λ is the flux density[3]. Doing such for both F105W and F160W filters, we retrieve the color of the image, i.e., the difference in magnitude in the F160W filter and in the F105W

[2]https://www.stsci.edu/hst/instrumentation/acs/data-analysis/zeropoints
[3]https://www.stsci.edu/hst/instrumentation/wfc3/data-analysis/photometric-calibration

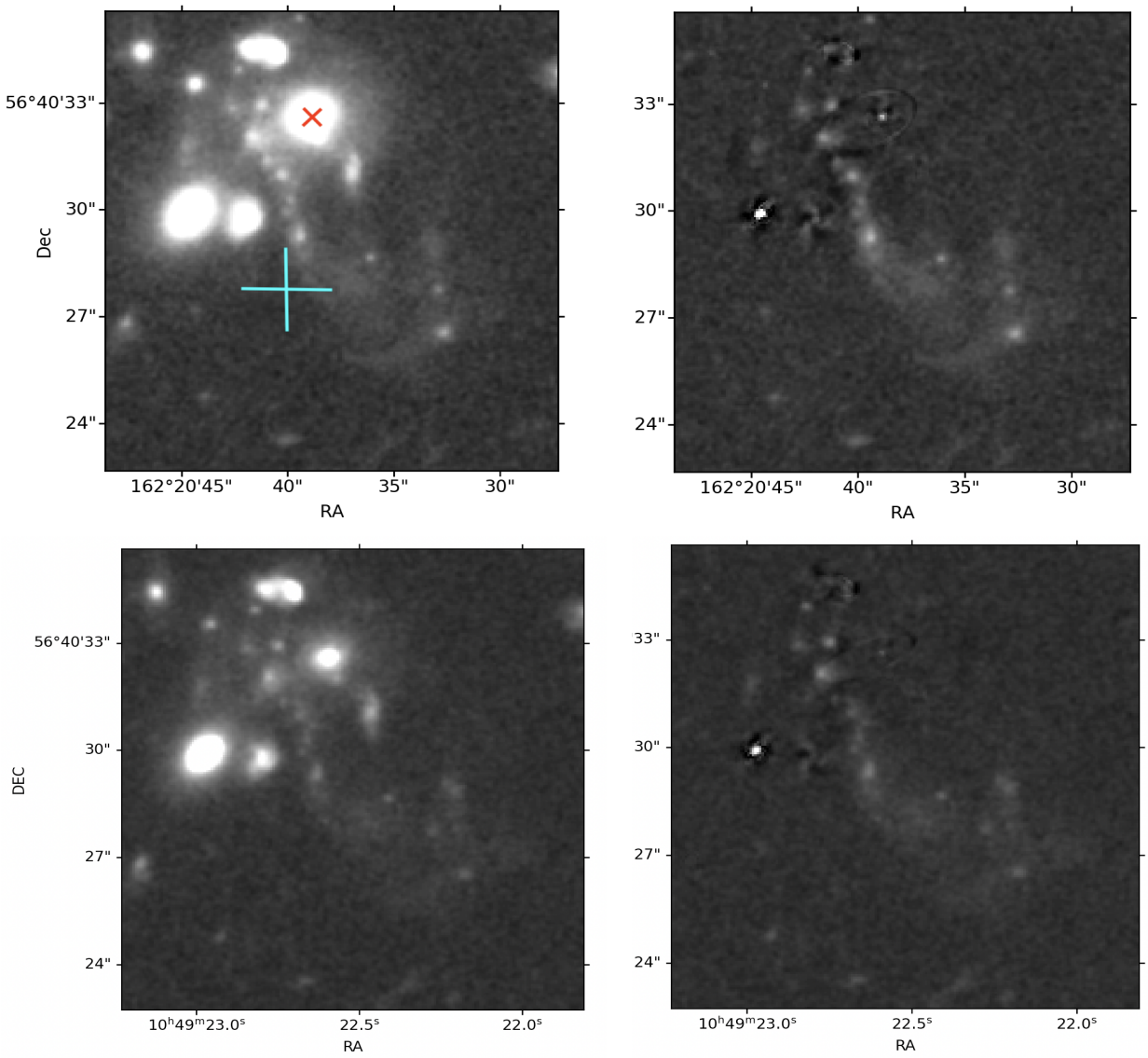

Figure 3.2: Top left: The original drizzled image of SpARCSJ-104922.6+564032.5 through the F160W filter. The position of the central galaxy is indicated by the red cross. The cyan cross shows the position of the center of the soft X-ray emission, and its size represents the positional uncertainty. Figure adapted from Barfety et al. in prep. Top right: The residual image after the galaxies were fit and removed. Bottom left: The original drizzled image of SpARCSJ-104922.6+564032.5 through the F105W filter. Bottom right: The residual image after the galaxies were fit and removed. The two residual images are the ones used in the analysis, after removal of the artifacts associated with the galaxies.

filter ($m_{F160W} - m_{F105W}$).

Deriving the mass-to-light ratios for each individual pixel can be done by using the relation between optical and NIR colors and stellar M/L as presented in Bell et al. 2003 [23]. The relation is expressed as:

$$\log_{10}\left(\frac{M}{L}\right) = a_\lambda + (b_\lambda * color). \tag{3.2}$$

where $a_\lambda = -0.223$ and $b_\lambda = 0.299$ are empirically determined parameters using rest frame u and r (SDSS)[4] - which roughly correspond to the redshifted F105W and F160W filters respectively -, and the *color* is the difference in ST magnitudes between the F105W image and the F160W one. The difference in color from the SDSS filters and HST filters is accounted for in the error estimation (§3.2.2). With a mass-to-light ratio in hand, it is possible to convert the observed F160W flux density to a stellar mass, taking into account cosmological dimming. The resulting mass-per-pixel map is shown in Figure 3.3. This map traces, but is not identical to, the F160W light map. The mass in the three brightest clumps of the tail is also measured, to determine if they could be recently formed dwarf galaxies. The results are presented in §3.3.

It should be noted that sky subtraction - one step of data reduction through AstroDrizzle - returned negative values for some of the background pixels in both HST images. This leads to errors when converting the data to magnitudes before getting the color. To overcome this

[4]http://skyserver.sdss.org/dr1/en/proj/advanced/color/sdssfilters.asp

issue, the steps described in the paragraph above were repeated twice, once on the absolute value of all the pixels in the image, and once on the absolute value of the pixels flagged as negative. The final mass value is then the difference between the sum of all the pixels in the mass pixel map (Figure 3.3) and the sum of the "negative" pixels.

3.2.2 Uncertainties in the Mass Estimate

There are several uncertainties inherent to the data or introduced into the measurement by the method outlined in the previous section.

- Despite the sky subtraction step in AstroDrizzle, background fluctuations are included in the error analysis. To do so, the area around the tidal tail of SpARCSJ-1049 is divided into 64 squares of 20x20 pixels; in which the pixel values associated to light sources are replaced by randomly chosen sky values. I proceed to compute the mean values of the pixels in each of the squares, and use the standard deviation of those 64 values as the uncertainty in the pixel values. This uncertainty can then be propagated to both the color and luminosity, and finally to the mass, using error propagation formulas. This amounts to an error of $< 1\%$ in the final mass measurement.

- Noise in the colour values lead to high M/L values for some pixels, which then transferred to high mass values. To estimate the magnitude of this effect, I set a threshold value above which the M/L of the pixel is deemed un-physical, and replaced by a background value. This threshold has a non-negligible impact on the

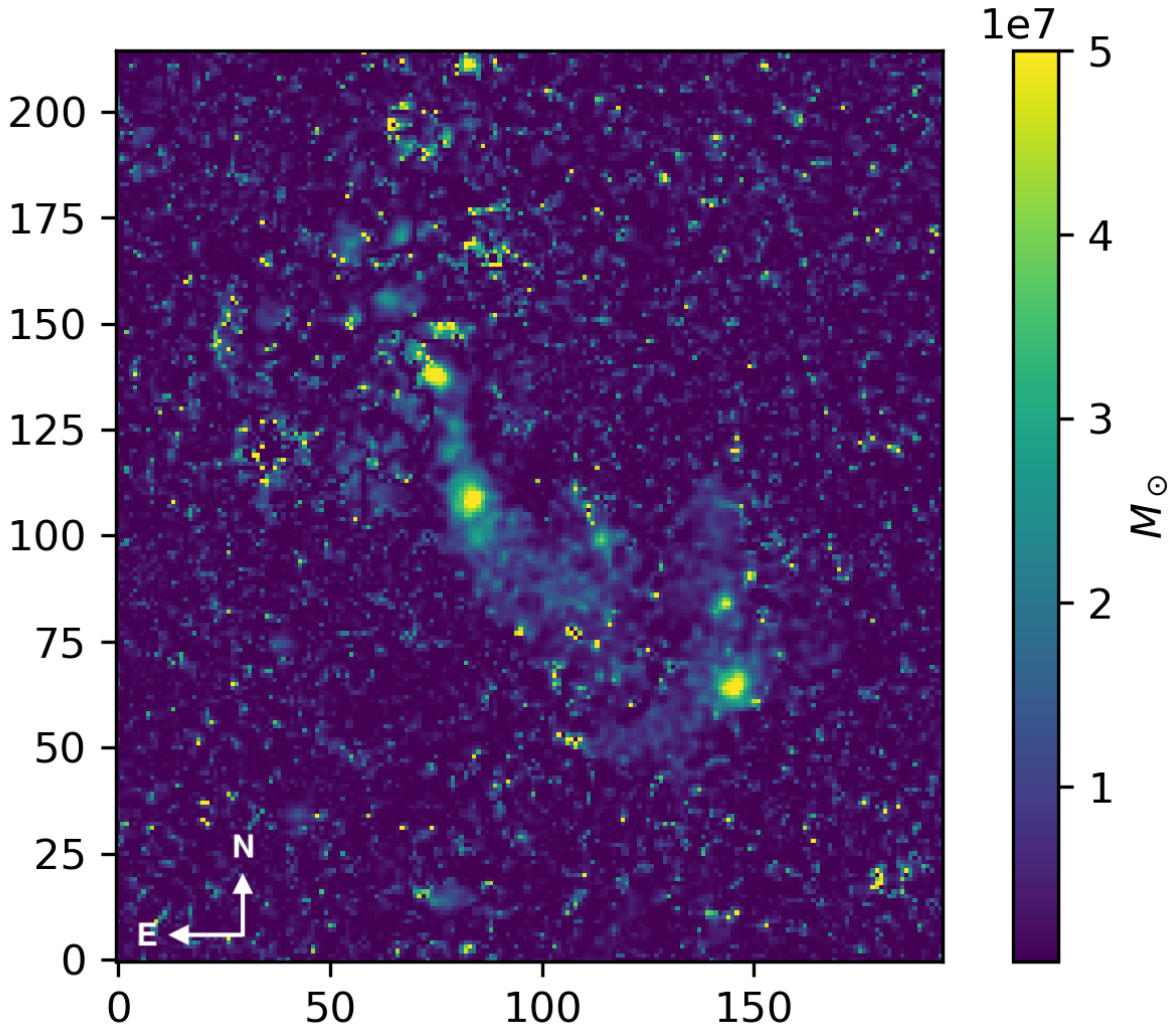

Figure 3.3: The above is a mass-per-pixel map of the area shown in Figure 3.2. The noisy pixels in the background are due noisy pixels with un-physical colours and the galaxy subtraction. These fluctuations are taken into account in the errors budget. Here we see the mass distribution is compressed into the tidal tail which extends roughly 65 kpc, and is composed of several large mass clumps. Figure adapted from Barfety et al. in prep.

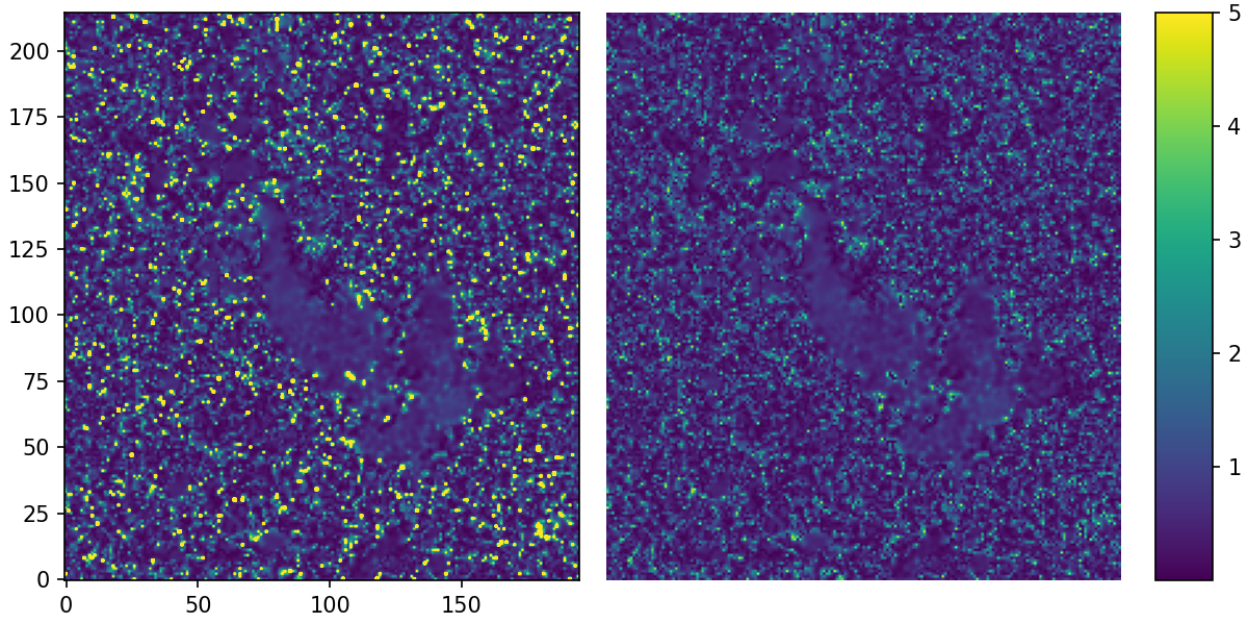

Figure 3.4: Comparison between the M/L pixel maps depending on the two extremes for threshold values. The left panel has no threshold, whereas the right panel has a threshold of 5, below which some of the mass in the tail is cut-off.

mass. By varying the value of the threshold from the lowest (using the minimum threshold below which physical mass in the tail is cut-off, shown in the right panel of Figure 3.4) to infinity (without a threshold, shown in the left panel of Figure 3.4), it is observed that the mass varies around $1 \times 10^{11}\ M_{\odot}$, with a scatter of 0.1 on this value, which is used as the uncertainty on the mass from this effect. This noise in the M/L thus introduces a 10% error in the mass value. It should be noted that Figure 3.3 displays the pixel map of the mass for a threshold value of 10.

- The M/L calculations were made using parameters determined with SDSS filters, while the data was recorded through HST filters. As filters do not have the same

characteristic wavelengths and response curves, this approach is expected to induce an offset in the color, which propagates to the measurement of the mass.

How this offset might influence the mass measurement is quantified by studying the difference in colors in HST and SDSS filters for 18 different galaxy SED templates (from Blanton & Roweis (2007) [52]; Coleman, Wu & Weeman (1980) [53]; Kinney et al. 1996 [54] and Grazian et al. 2006 [55]), which cover a wide range of SEDs. The color estimation is done the following way: the spectra of the 18 templates are interpolated onto the four filters' (F160W & F105W - corrected to redshift 1.71 - and rest frame SDSS u & SDSS r) response curves, to mimic the detection of the galaxy by the filters. Integrating the resulting curve over the wavelength range of the filters returns a total flux, one per filter. From this, it is possible to get the colors – $(m_{F160W} - m_{F105W})$ and $(m_u - m_r)$ – and the difference between the two colors is the offset induced by the difference in filters.

Those 18 color offsets are added to the color pixel map, computed in §3.2.1 using the SpARCSJ1049 images, and the resulting mass is measured using the method described in §3.2.1. These masses are shown in Figure 3.5 (blue stars). The standard deviation of these mass values is used as the uncertainty characterizing the effect of filter offset on the final mass estimate (Figure 3.5, dotted red lines). Using the 18 SED templates, there is an estimated 17% error introduced in the mass by the offset between HST and SDSS filters.

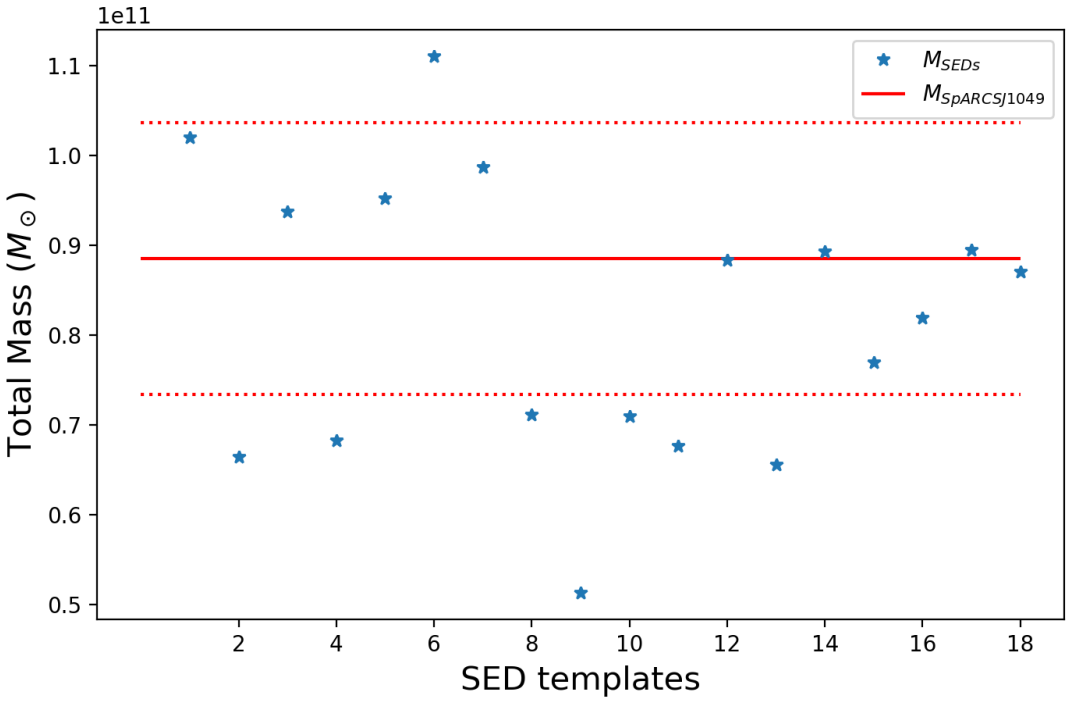

Figure 3.5: Variation in the total mass of the area when taking into account filter offsets for each of the 18 SED templates. The red line is the total mass derived from the HST imaging. The dotted lines are the error in the total mass based on the standard deviation of the mass offsets.

3.3 Results

Following the method described previously, the total stellar mass in the region is estimated at $M = (1.00 \pm 0.18) \times 10^{11}\ M_{\odot}$. The scatter in Equation 3.2 also introduces an average systematic error of $\sim 40\%$ (Bell et al. 2003 [23]). The three brightest clumps in the tail have stellar masses (from top to bottom) $1.76 \times 10^{9}\ M_{\odot}$, $2.04 \times 10^{9}\ M_{\odot}$ and $1.93 \times 10^{9}\ M_{\odot}$; which indicates that they are most likely dwarfs galaxies formed by the intense star formation. However, they only amount to $\sim 6.4\%$ of the total stellar mass measured in the area.

Using the estimated mass of the BCG $M_{BGC} = (3.0 \pm 0.5) \times 10^{11}\ M_{\odot}$ from Webb et al. 2015b [7], the total BCG+ICL mass in the $12.9'' \times 11.7''$ region is $M_{BCG+ICL} = (4.00 \pm 0.53) \times 10^{11}\ M_{\odot}$. This number is very close, but not in complete agreement, with the estimate of the stellar mass inside a 100 kpc aperture centered on the BCG by DeMaio et al. 2020 [18]: $M = (4.97 \pm 0.48) \times 10^{11}\ M_{\odot}$.

Chapter 4

Evolution of the ICL in the SpARCS Clusters

This chapter investigates the redshift evolution of the ICL in a sample of $\sim$ 890 SpARCS clusters, spanning $0.175 \leq z \leq 1.9$. The clusters were observed by DECam as part of the Dark Energy Survey (DES). The chapter investigates the process of retrieving a central galaxy (CG) + intra-cluster light (ICL) light profile for all clusters, through the masking of foreground/background objects and the stacking of clusters at similar redshift to maximise the SNR. The analysis in the section was realized, and written, exclusively by C. Barfety.

4.1 The SpARCS Clusters in the Dark Energy Survey

4.1.1 SpARCS Clusters

The sample of clusters used for the analysis comes from the SpARCS catalogs (Wilson et al. 2009 [46], Muzzin et al. 2009 [47], Demarco et al. 2010 [48]). The DES survey covers the entirety of the southern fields of the SWIRE Legacy Survey Fields. This amount to a total of 1367 clusters, with photometric redshifts spanning $0.175 \leq z \leq 1.9$. The clusters are identified by detecting overdensities of galaxies in the red-sequence.

Before any analysis or image processing is conducted, the SpARCS catalogs are used to triage the clusters, and maximise the number of detections by DECam. The sample is first reduced to 1118 clusters by discarding all clusters detected too poorly to insure they are in fact clusters; using a signal-to-noise proxy for the goodness of the detection. In addition, visual inspection of the clusters one-by-one, before any masking, purged the sample further from false detection, where the "BCG" is in fact a star, or if a particularly bright object in the vicinity of the "cluster" skewed the color of the region. This brings the sample to 889 clusters.

The richness distribution of the cluster sample is shown in Figure 4.1, as a function of redshift. The sample is roughly even over the whole sample, indicating that the same population of cluster is probed throughout the survey. This is likely a selection effect of the survey: identifying clusters through their overdensity in the red-sequence will tend to

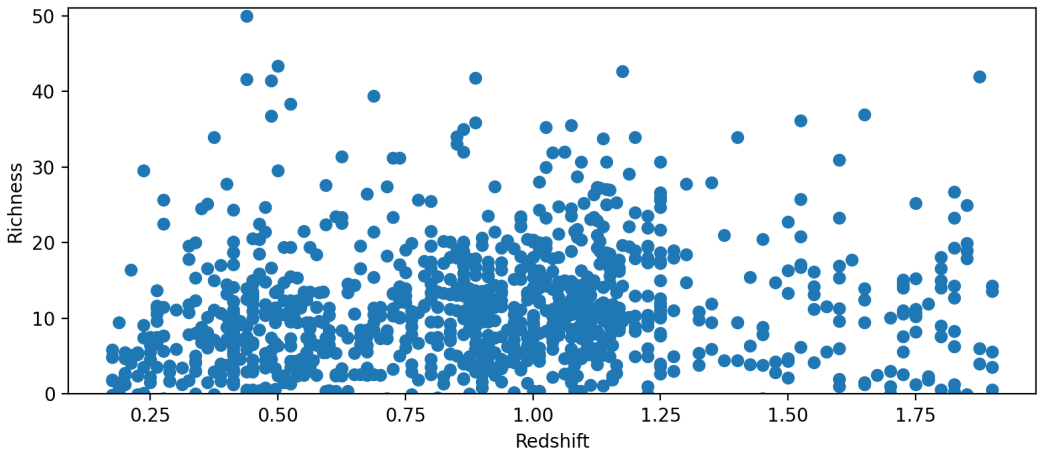

Figure 4.1: Cluster richness distribution as function of redshift. The distribution is roughly even at all redshifts, indicating a similar mass range across the whole range.

detect only clusters with large masses at higher redshift. Using the results from Andreon & Congdon 2014 [56] to convert cluster richness into cluster mass; the mean cluster mass inside 500kpc of the sample is $M_{500kpc} = (1.8 \pm 0.5) \times 10^{14}\, M_{\odot}$.

4.1.2 DES Imaging

The Dark Energy Survey is a photometric survey of the Southern Sky, begun in 2013, using the DECam instrument on the Blanco 4m telescope at the Cerro Tololo Interamerican Observatory in northern Chile. While the survey uses all five *grizY* filters, only the two reddest z and Y are considered in this study, as the ICL is thought to be rather red. The difference in wavelengths due to redshift are accounted for using evolutionary and k-corrections (§4.2.3). Both filters have peak sensitivity at 9260 Å and 10,095 Å

respectively. In 2021, the DES collaboration published their second data release (hereafter DR2 [57]), which is the release used in this work. The exposure time for z filter co-added images is 990s, and and 585s for Y filter images, with median coadded depth of 23.1 and 21.7 mag for the z and Y filter respectively. The magnitude zero-point for all filters has been calibrated to be 30 mag/s (DES Collaboration 2021 [57]).

The images used here are retrieved through the NCSA DESaccess service[1]. The size of the cutouts are tailored as a function of the redshift of the cluster to ensure that the images include at least a 500kpc radius around the central coordinates. They are available in the form of FITS files, with three extensions: the science image (SCI), a bad pixel mask (MSK), as well as an inverse-variance weight map (WGT). These are the final product of the DES image processing pipeline, described thoroughly in Morganson et al. 2018 [10]. The files are processed a first time to form what are called the Final Cut images. These are single-epoch images that underwent a first background subtraction, bad pixel masking, flat field correction, etc. Then, the Final Cuts go through a new processing, where overlapping images are co-added together to form multi-epoch images. For the purpose of this work, the steps in the processing which influence the analysis the most are briefly reviewed here. These are the single-epoch background subtraction, the co-adding of single epoch images using SWARP, as well as the creation of the inverse-variance images.

[1]https://des.ncsa.illinois.edu/desaccess/

Background Subtraction Pipeline

In the first part of the image processing, the single epoch images undergo a first sky subtraction. This sky subtraction is as follows: the pipeline create four sky templates, using different Principle Component Analysis (PCA) components. The four templates are the following: a median image with a large scale scattered light torus and a small scale fringe pattern, two smooth orthogonal gradients, and another image including the pupil and fringe patterns with different ratios than the first image. These four templates are created both in high and low resolution. After that, the science images are binned in the same resolution (128×128 blocks of pixels) as the low-resolution templates, and are fitted with those four templates. The results of the fits are multiplied to the high-resolution PCA templates, producing a model for the sky background which is then subtracted to the high-resolution science images. Finally, the image is divided by a "star flat" image to take into account the difference between the flux response and the dome flat. This algorithm is described in detail in Bernstein et al. 2017 [58] and Morganson et al. 2018 [10], and was estimated by the authors to have a very small impact on extended and diffuse components.

Co-adding Process

After the first processing of the images from the CCDs, those files are co-added together to form multi-epoch science images, which is done using the SWARP software (Bertin et al. 2010 [59]). The exact parameters used are described in Table 23 of Morganson et al.

2018 [10]. As it is not possible to process the whole 5000 $\deg^2$ at once, the DES area is divided in $10,000 \times 10,000$ pixel tiles, in which all the exposures of that region are combined together. Each exposure taken by SWARP as input is composed of four extensions: the flux image in electrons/pixel, a bad pixel and cosmic ray mask, and two weight images with different weighting approaches (one more conservative than the other). The creation and processing of the weight maps is described in the following subsection.

During the combining by SWARP, the software also includes a background estimation and subtraction. This process can affect the measurements as it can over-subtract the sky surrounding bright objects, which in this case can lead the subtraction of the ICL. This is investigated in more detail in §4.2.4.

Inverse-Variance Maps

The Inverse-Variance Maps (IVM) used in this study are extensions in the FITS files provided by the NCSA DESaccess service. These are the produce of SWARP, which itself uses the single-epoch IVM produced in the Final Cut pipeline (Morganson et al. 2018 [10]). The single epoch weight maps come from the inverse-variance in photoelectrons in the fitted sky model from the PCA templates. The weights map are then used as inputs for SWARP, which uses them to create both the co-added science image and the output weight file.

This final inverse-variance output is used in the analysis as the pixel-by-pixel uncertainty, which is propagated through the data analysis steps.

4.2 Methods

Since the ICL is so diffuse, its measurement can be very delicate, especially as the redshift increases. This is why many careful steps are to taken to ensure a measurement as devoid of external contamination as possible, while maximizing the potential signal. This section describes and illustrates the different stages of the analysis: 4.2.1 explains the masking and stacking process the images undergo, while §4.2.2 goes over the light profile estimation for the clusters. §4.2.3 and §4.2.4 investigate the k-correction and the effects of background subtraction on the curves of growth respectively, while §4.2.5 converts an ICL light profile from the literature to the bandpass used in this analysis for comparison. Finally, §4.2.6 estimates the depth of the stacked profiles, and §4.2.7 goes over the potential influence of the PSF.

4.2.1 Masking and Stacking

For the purpose of this analysis, masking is one of the most - if not the most - crucial step of the process. Indeed, masking must be efficient enough to cover most of the light related to sources in the regions (in particular coming from cluster galaxies), but not generous enough that it would encompass some of the intra-cluster light. It should be noted that since the delimitation between the BCG and ICL is almost impossible to determine with precision, and would introduce additional uncertainties in the measurements, the BCGs are not masked out of the images, and both components are treated as one. Any analysis is made on the

basis of distance from the cluster center.

For each set of cluster, there are two main components needed for the masking: the coordinates of the BCG, from the SpARCS catalogs; and the inverse-variance image of the file, described in §4.1.2. With those two parameters as input, the source detection software SEXTRACTOR (Bertin et al. 1996 [60]) creates a catalog of all the sources in the image. The inverse-variance map here serves as a weight image keeping the number of false detection to a minimum. For each detected source, all the pixels inside a radii of 3.5 x Kron radius, the first moment of the surface brightness profile as computed by SEXTRACTOR, are masked as it is estimated that it encompasses more than 90% of a galaxy's light (Kron et al. 1980 [61], Zhang et al. 2019 [11]). The result is shown in Figure 4.2 for a cluster at $z = 0.338$. All sources are masked, except for the central galaxy, hereafter referred to as the BCG. We note that there is some visible residual light around one of the sources in the top right panel of the image. The source might be a star, whose light profile is not well characterized by the Kron radius, and thus some residual flux is to be expected in the masking. This effect is counteracted by the background subtraction presented in §4.2.4, and clusters with stars in the inner 100 kpc were discarded in the visual inspection (§4.1.1).

Lastly, an extra step is added in the masking to account for the masked regions. An extension is created in the corresponding FITS files, acting as a "weight" file of the image, where each masked pixel is attributed the weight 0, and each non-masked pixel is attributed the value 1.

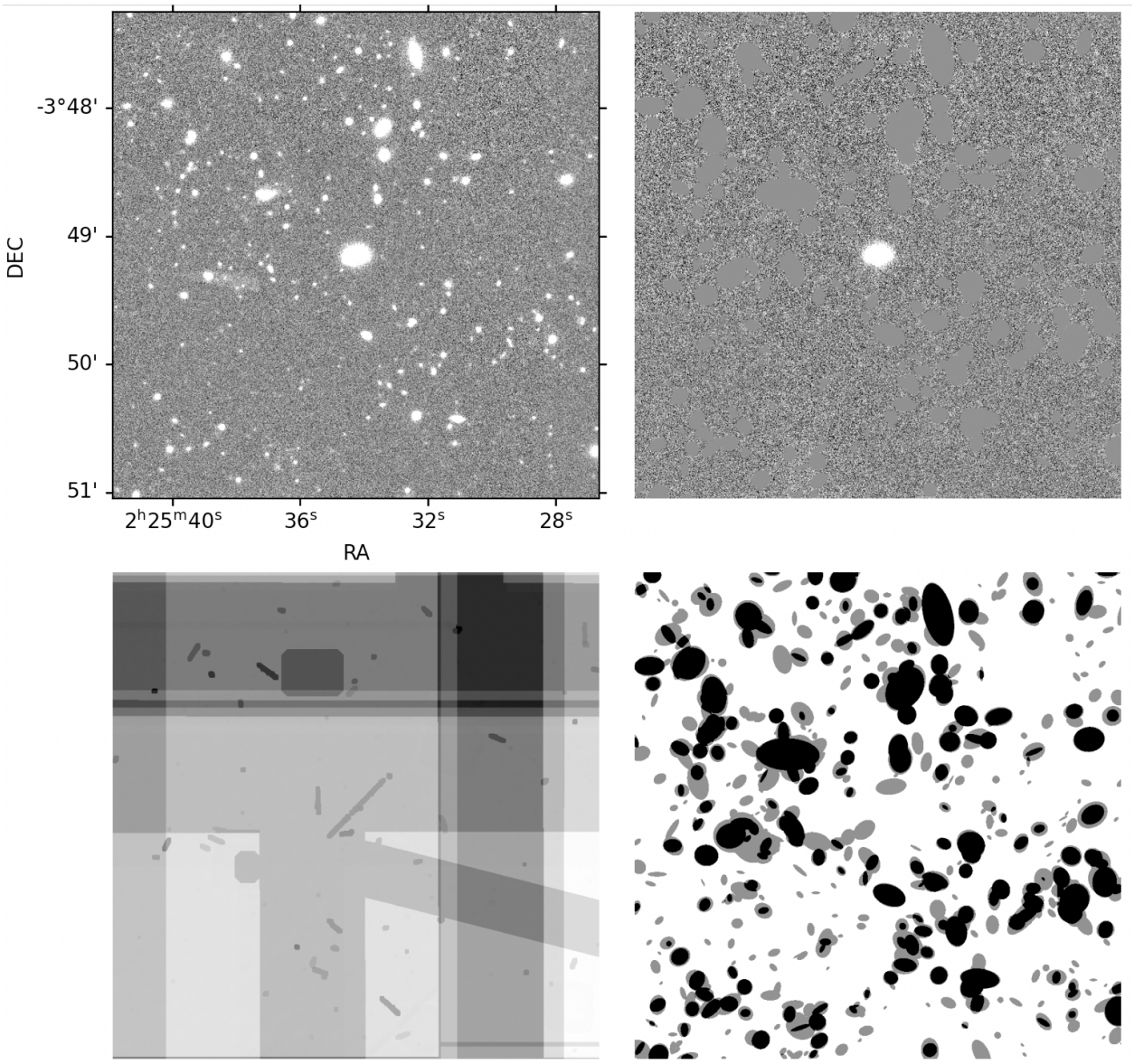

Figure 4.2: Image processing example for a cluster at $z = 0.338$. On the top left is the co-added z filter image from DR2, while the top right is the masked and combined z and Y band image, and the image used to retrieve the light profile. The bottom left is the combination of the inverse-variance maps from both filters as given by DES, described in §4.1.2, and the bottom right panel is the weight map created in the masking process (which shows all the apertures masked in the process) to account for the masked pixels in the flux estimation, described in §4.2.1

Once the images from DECam's z and Y filters are properly masked, they are stacked together, with the goal to maximize the amount of flux perceived for each cluster. This operation is relatively straight-forward, as it only requires to average both filter images for each cluster. For the example cluster shown in Figure 4.2, the stacked product is displayed in the top right panel. Such average is also performed on the weight maps created in the previous masking step, as the images from both filters have different sensitivity, and thus might not have the exact same pixels masked. This returns a new weight image for the stacked files of the cluster, with values 0, 0.5, and 1. The resulting weight map is displayed in the bottom left panel of Figure 4.2. As for the inverse-variance maps, they are treated as statistical error maps, and are combined together using error propagation formulas (bottom left panel of Figure 4.2).

4.2.2 Light profile Estimation

For each cluster, the analysis focuses on the light inside a 500 kpc radius around the BCG's coordinates. Moreover, since in most cases it is not possible to clearly distinguish the limit between the BCG halo and the ICL, there is no attempt to separate the two components. Any feature is referred to by its distance to the cluster, starting from 1kpc.

The light profile is extracted the following way: annuli of width 5kpc and of increasing radii are used to measure the total flux coming from the images, in counts/s. As a result of the masking process described in §4.2.1, all pixels have an attributed weight of 1, 0.5,

or 0; the latter also having a flux value of 0, as they are completely masked. To take this into account when computing the flux in each annuli, the value of all fully masked pixels is replaced by the mean of the un-masked pixels, and their corresponding error in the IV map is replaced by the standard deviation of this mean. Similarly, the pixels with weight 0.5 (eg: when the contours of the masked source was different in both filters) are added with half the mean of the un-masked pixels; and the error is added in quadrature with half of the standard deviation. The final flux is then the sum of all pixels in the annuli, and the final error is the sum in quadrature of all the pixel errors.

This returns 101 values of flux between 1 and 500 kpc. An additional step taken here is the subtraction of the cluster's light profile by an average background light profile, to minimize contamination by any residual light. At the same time, the error in each flux value computed above is combined with the error in the mean from the background estimation. The process of creating this background profile is explained in detail in §4.2.4, and the resulting background subtracted light profile is shown with its errors in red in Figure 4.3.

Then, by equating Equation 4.1:

$$m = -2.5 \log_{10}(F) + 30.0, \tag{4.1}$$

where 30.0 is the magnitude zero-point of the images in mag/s as given by the DES collaboration for the second data release (Abbott et al. 2021 [57]); with the equation for AB magnitudes (Oke & Gunn 1983 [62]):

$$m_{AB} = -2.5log(f_\nu) - 48.6 \tag{4.2}$$

where f_ν is the flux density; it is possible to retrieve the flux density, in units of erg/s/cm^2/Hz.

Now, to make an adequate comparison between the clusters' light profiles, the observed flux must be converted to emitted luminosity. Doing so means accounting for various effects due to redshift, which can be done using the following equation from Oke & Sandage 1968 [63]:

$$m_{obs} = M_{rf} + DM + K \tag{4.3}$$

where K is the k-correction, reviewed in detail in §4.2.3; m_{obs} is the observed apparent magnitude; DM is the distance modulus; and M_{rf} is the rest-frame absolute magnitude.

Expressing Equation 4.3 in units of flux, it becomes:

$$-2.5\log(f_\nu(\nu_o)) + 30 = -2.5\log\left(\frac{L_\nu(\nu_e)}{4\pi 10^2}\right) + 30 + 5\log\left(\frac{D_L}{10}\right) + K$$

$$\rightarrow f_\nu(\nu_o) = \frac{L_\nu(\nu_e)}{4\pi D_L^2} 10^{-K/2.5} \tag{4.4}$$

where D_L is the luminosity distance, computed for each cluster with their photometric

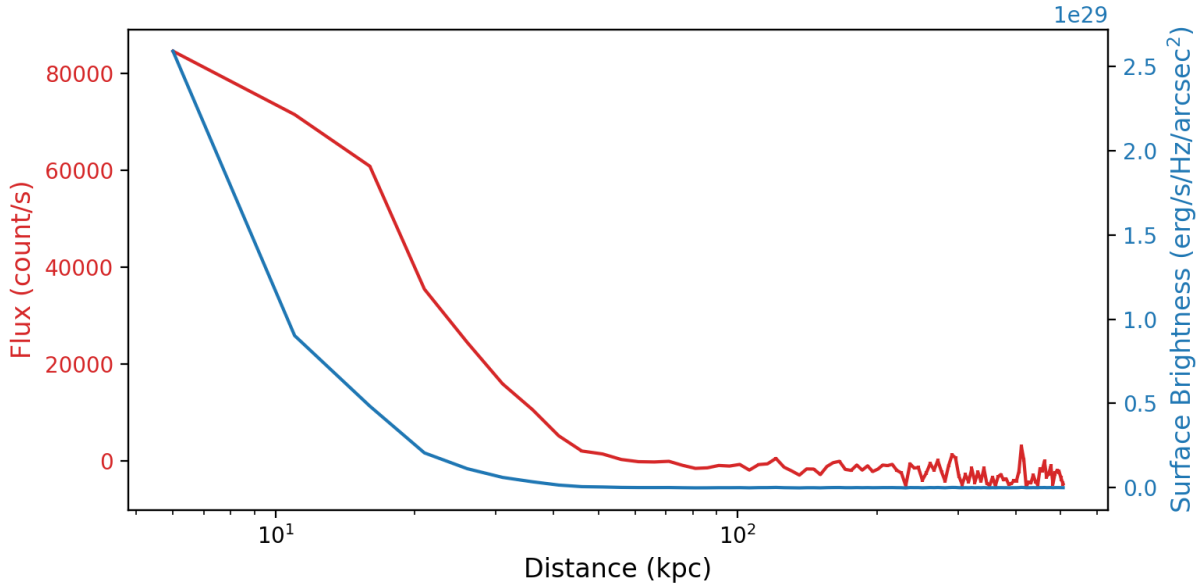

Figure 4.3: Background subtracted light profile of the $z = 0.338$ cluster shown in Figure 4.2 as directly retrieved from the image (blue), compared to the final product in surface brightness after the conversion presented in §4.2.2 (red). Error bars from the IVM and the background subtraction are included, but are too small to show.

redshift; f_ν is the observed flux; and L_ν is the emitted luminosity in erg/s/Hz. For this part of the analysis, the k-correction is computed using the Bruzual and Charlot 2003 [64] stellar population models, with a Chabrier IMF (Chabrier 2003 [65]) and solar metallicity. Moreover, since the images used to retrieve the light profiles are stacked images from the z and Y band, a new filter response function is created to compute the k-correction. This new response curve is the same as the z and Y filter on the wavelengths where they do not overlap, and the average transmission of both where they do overlap.

Finally, the last step of the analysis is to take the emitted luminosity per unit area, i.e.

divide by the area of each annuli, to obtain the surface brightness in erg/s/Hz/arcsec^2. This final product is shown in blue in Figure 4.3.

Stacked Profiles

The method described above retrieves a light profile for each cluster. However, based on the exposure time of the files, and because those are ground-based images; the data are not deep enough to detect the ICL. Stacking the profiles is therefore an efficient way to counter this. In this analysis, the profiles are stacked in five redshifts bins which appear to span an important epoch in the formation of the ICL: $0.2 \leq z \leq 0.3$, $0.5 \leq z \leq 0.6$, $0.7 \leq z \leq 0.8$, $1.0 \leq z \leq 1.2$ and $1.5 \leq z \leq 1.6$.

Once again, the stacking is relatively straightforward. All the profiles of the clusters inside one given bin are averaged to form a general profile with maximum SNR in the given redshift bin, weighting each profile by its measured error. The results are shown in Figure 4.8. The errors for the averaged profiles are computed using the jackknife resampling method. This method consists in the following: for a sample of N values, N sub-samples are created, with all the values of the original sample except for n^{th} value of the sample. This returns N sub-samples of length N-1. The statistical property of choice can then be evaluated for each of the sub-samples (in the case, the average). This returns N light-profiles, averaged over N-1 original profiles. It is then possible to compute a bias-corrected estimate of this average, using:

$$\overline{\theta}_{jack} = \overline{\theta} - \overline{bias}, \tag{4.5}$$

where $\overline{\theta}$ is the average of the original sample; and $\overline{bias}$ is the difference between the average of the sub-sample averages computed above and $\overline{\theta}$, multiplied by the number of degrees of freedom (Efron 1982 [66]). Finally, the standard error in the jackknife estimate is computed using[2]:

$$\sigma_{jack} = \sqrt{\frac{1}{N(N-1)} \sum_{i=1}^{N} (\theta_{jack,i} - \overline{\theta}_{jack})^2}. \tag{4.6}$$

This estimate for the standard error is used as the uncertainties on the light profiles displayed in Figure 4.8.

4.2.3 K-correction

As mentioned above, redshift has various effects on astronomical observations, some of which are quantified - and corrected - by the K-correction. This quantity is the difference in magnitude between the rest-frame bandpass and the observer bandpass, and takes into account two effects: 1) the redshifting of the filter's wavelength, expressed by $\nu_e = (1+z)\nu_o$; and 2) the change in the portion of the SED sampled by the redshifted filter.

[2]https://math.montana.edu/jobo/thainp/jack.pdf

While the original K-correction accounted solely for redshifts effects in a single bandpass (Humason, Mayall & Sandage 1956 [67], Oke & Sandage 1968 [63]), a generalized form of the correction, allowing for any shapes and positions in the filters, is derived in Hogg et al. 2002 [68]. The correction can be expressed as:

$$K = -2.5\log_{10}\left[(1+z)\frac{\int \frac{d\nu_o}{\nu_o} R(\nu_o) L_\nu(\nu_o[1+z])}{\int \frac{d\nu_o}{\nu_o} R(\nu_o) g_\nu^R(\nu_o)} \frac{\int \frac{d\nu_e}{\nu_e} Q(\nu_e) g_\nu^Q(\nu_e)}{\int \frac{d\nu_e}{\nu_e} Q(\nu_e) L_\nu(\nu_e)}\right] \tag{4.7}$$

where $R(\nu)$ and $Q(\nu)$ are the response functions of the observer frame filter R and rest-frame filter Q, L_ν is the emitted-frame luminosity, and $g_\nu^{R,Q}$ are the SEDs for the zero-magnitude source. It should be noted that this analysis only uses DECam filters, which have been calibrated to have the same zero-point, hence simplifying the above equation to:

$$K = -2.5\log_{10}\left[(1+z)\frac{\int \frac{d\nu_o}{\nu_o} R(\nu_o) L_\nu(\nu_o[1+z])}{\int \frac{d\nu_e}{\nu_e} Q(\nu_e) L_\nu(\nu_e)}\right] \tag{4.8}$$

This can be decomposed into:

$$K = -2.5\log_{10}\left[\int \frac{d\nu_o(1+z)}{\nu_o} R(\nu_o) \frac{L_\nu(\nu_o[1+z])}{4\pi 10^2}\right] + 2.5\log_{10}\left[\int \frac{d\nu_e}{\nu_e} Q(\nu_e) \frac{L_\nu(\nu_e)}{4\pi 10^2}\right]$$

Which is simply the difference between the absolute magnitude through the observed bandpass and the absolute magnitude through the emitted bandpass: $K = M_{R,obs} - M_{Q,rf}$.

In the event that the spectral energy distribution is flat, then Equation 4.7 reduces

to $K = -2.5\log_{10}(1+z)$, which, when injected into Equation 4.4, retrieves the familiar expression relating flux and luminosity for a source at redshift z (Hogg et al. 1999 [69]):

$$S_\nu(\nu_o) = (1+z)\frac{L_\nu(\nu_e)}{4\pi D_L^2}.$$

4.2.4 Background analysis

Background Subtraction by SWARP

There are multiple aspects to the background subtraction in this analysis. First of all, because of the nature of the ICL, i.e. the fact that it is very diffuse on large scales; it is very sensitive to background subtractions such as the one from the SWARP software (Bertin et al. 2010 [59]). This background subtraction is done by splitting the field in a rectangular grid, where each rectangle has a size defined by the user (in this case, the box size is 256 pixels). Within each mesh, the background is estimated by clipping the mean pixel value until the mode is within 3σ of the median. The meshes are then related to one another using bicubic-spline interpolation, creating a final background map which is subtracted to the science image. While this technique is very efficient, in the case of diffuse halos, if the box size is comparable or smaller in scale than the ICL, the halo is very likely to be interpreted as background fluctuations and subtracted off.

To estimate whether this effect might influence the measurement of the ICL in this study, the physical size of the box chosen by the DES collaboration in the data processing pipeline

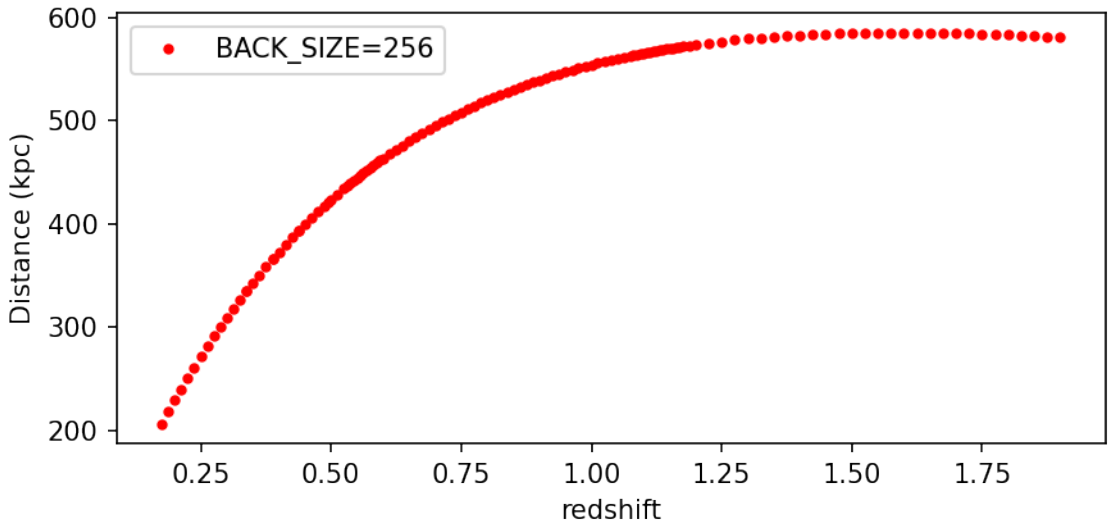

Figure 4.4: Physical size of the box used by SWARP to estimate and subtract the background as a function of redshift, for a pixel scale of 0.263 ”/pixel. The box size parameter, BACK_SIZE, is 256 pixels, the value disclosed in Morganson et al. 2018 [10].

is investigated. The results are shown in Figure 4.4. As the figure shows, for higher redshifts, the background box is $\sim 600 \times 600$ kpc^2. In this situation the box is sufficiently large that variations in the background flux due to the ICL are not over-subtracted. At intermediate redshift, this effect is still negligible, but the lower redshift clusters, below $z = 0.25$ might suffer from this background subtraction. The effects of this are evaluated by inspection of the integrated flux in §4.3.2.

Average Background Light Profile

Another aspect of the importance of background subtraction in the images is residual light. Indeed, while the images undergo a thorough masking process, there is bound to be some

residual light from nearby galaxies, or stars. To counteract this effect as much as possible, a simulated average background light profile for each clusters is produced using random points.

To this purpose, 50 sets of coordinates are randomly generated in a region between 1 Mpc and 10 Mpc around each of the 889 clusters. The lower limit is so that the light profile from a random point does not overlap the light profile from the cluster, while the upper limit is to insure that the two points are sufficiently close to share a similar background. For each of the random coordinates, the corresponding images in the z and Y bands are downloaded, and undergo the same process as the cluster images (i.e. masking of all the sources, stacking, light profile estimation), up until the retrieval of the raw light profile from the image. The 50 background light profiles for the cluster shown in Figure 4.2 are displayed in black in Figure 4.5.

Once this is done for the 50 random points associated with one cluster, the average profile of those points is made - as well as the corresponding error in the mean - and is subtracted to the corresponding cluster. Doing so corrects for most of the background issues in each image, and returns light profiles as clean as possible. The average profile for the example cluster is shown in blue with its errors in Figure 4.5.

4.2.5 Comparison to Observed ICL Profile

In a previous study, Zhang et al. 2019 [11] made a detection of the ICL at $z = 0.25$ using clusters found in the DES survey, by stacking 280 cluster light profiles together. One of the

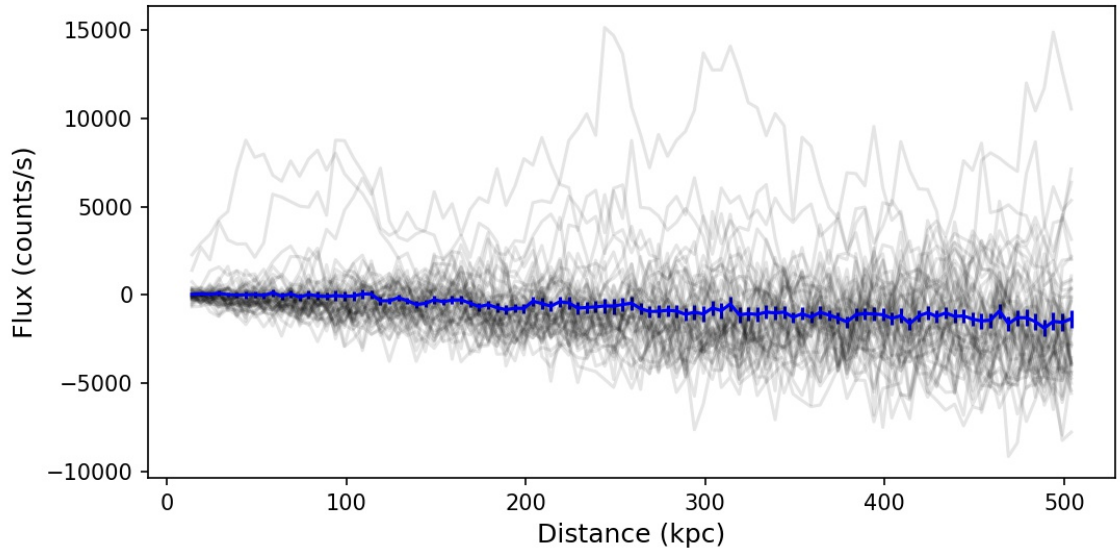

Figure 4.5: Curves of growth of the 50 random points associated to the cluster displayed in Figure 4.2 (black lines). In blue is the mean background curve, with the error in the mean in each point as error bars. The blue curve is then subtracted to the light profile from the cluster, which returns the profile shown in Figure 4.3.

	I_e $flux/arcsec^2$	n	Re kpc
Sersic 1	9830	1.34	9.13
Sersic 2	8846	3.07	52.1
Sersic 3	9.1	2.1	2600

Table 4.1: ICL profile parameters from Zhang et al. 2019 [11] for all three Sersic profiles, following Equation 4.9.

component of their analysis consists in fitting their BCG+ICL profile with the combination of three Sersic profiles, which describe the relation between the light intensity of a galaxy with the radius as:

$$I(r) = I_e \times exp\left(-b_n\left[\left(\frac{r}{R_e}\right)^{1/n} - 1\right]\right) \tag{4.9}$$

where R_e is the effective radius - or half-light radius -, which is the radius which encompasses half of the light emitted by the galaxy; n is the Sersic index; b_n is a parameter dependant on the Sersic index, which follows $\gamma(2n, b_n) = \frac{\Gamma(2n)}{2}$; and I_e is the intensity at R_e (Sersic 1963 [70]).

The best fit parameters of the study, used for comparison here, are shown in Table 4.1, and the resulting profile is shown as the dash-dotted curve in Figure 4.6. The intensity is already calibrated to the zero-point of DECam.

Now, there are a few factors to take into account before comparing this profile to the profiles extracted in this study. First of all, the curve from Zhang et al. 2019 [11] is given in units of flux/arcsec^2, and must therefore be converted to emitted luminosity. Secondly,

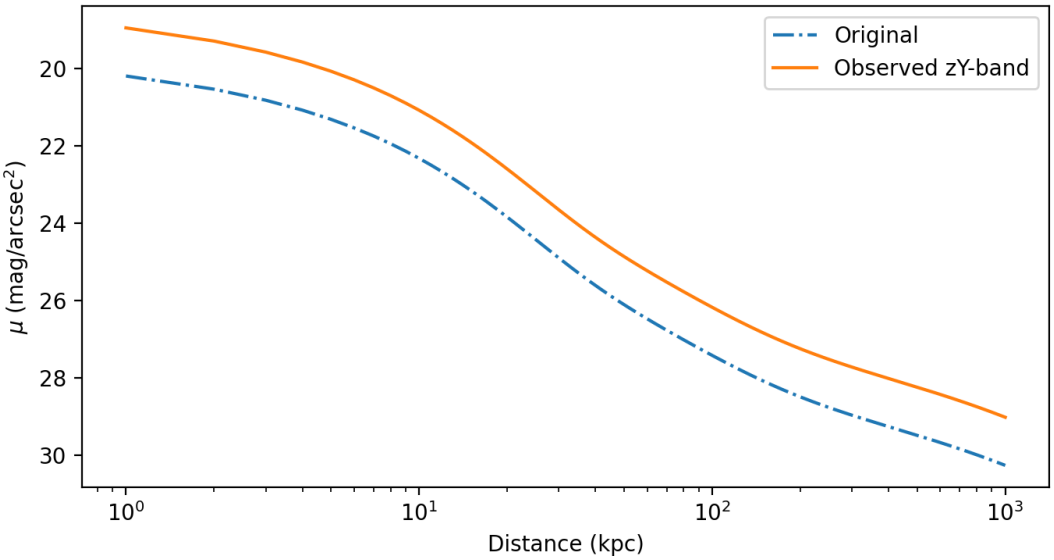

Figure 4.6: Reconstructed surface brightness profile of the ICL at $z = 0.25$ using the best parameters in Table 4.1 (Zhang et al. 2019 [11]). The dash-dotted curve is the original profile (i.e.: (e+k) corrected, in the r-band), while the orange curve is the profile converted to the observed zY-band.

this profile has been fitted on a profile extracted from r-band images, in opposition to the z and Y bands used in this study. Finally, the profile has not only been k-corrected, but e-corrected as well. The e-correction corrects for the evolution of the stellar population as a function of redshift, i.e. taking the galaxy and "evolving" it to $z = 0$. This correction is a difference in magnitude, similar to the k-correction; and the two are computed as one in Zhang et al. 2019 [11], using a stellar population model with metallicity $Z = 0.008$ and a single burst of SF at $z = 3$. This correction has to be "undone", in order to convert the observed r-band profile to an observed zY-band one.

Going back to the observed r-band profile from the corrected one can be done using the surface brightness version of Equation 4.3, only including the e-correction:

$$\mu_{R,obs} = \mu_{R,[e+k]} + [e + k](z) \tag{4.10}$$

where $\mu_{R,[e+k]}$ is the rest-frame surface brightness of the profile aged to today.

Then, converting from observed to rest frame:

$$\mu_{R,rf} = \mu_{R,obs} - 2.5\log_{10}(1 + z)^4 - k_{Robs,Rrf}(z) \tag{4.11}$$

where $k_{Robs,Rrf}(z) = M_{R,obs}(z) - M_{R,rf}(z)$ is the k-correction from the Bruzual & Charlot models and $2.5\log_{10}(1+z)^4$ is the familiar cosmological dimming term (Burke et al. 2015 [2], Furnell et al. 2021 [4]).

Combining the two we get:

$$\mu_{R,rf} = \mu_{e+k} + M_{R,rf}(z) - M_{R,ne}(0) - 2.5\log_{10}(1+z)^4 \tag{4.12}$$

Finally, the last conversion to go from rest-frame r-band to observed zY-band is done by using the surface brightness equivalent to Equation 2 from Hogg et al. 2002 [68]:

$$\mu_{zY,obs} = \mu_{R,rf} + 2.5\log_{10}(1+z)^4 + k_{zY,R}(z) \tag{4.13}$$

where $k_{zY,r} = M_{zY,obs} - M_{r,rf}$ is computed using the values from the GALAXEV stellar population models assuming a Charbier IMF (Chabrier 2003 [65]) and solar metallicity (Bruzual & Charlot 2003 [64]). This equation is simply the generalization for all bandpass of Equation 4.3 from Oke & Sandage 1968 [63].

4.2.6 Surface Brightness Detection Limit

As described in §2.1.1, a common way to define the ICL is to declare all the excess flux below a certain surface brightness threshold as intra-cluster light. A common value for this threshold is 26 mag/arcsec^2 in the rest-frame r-band (Krick & Bernstein 2007 [71], Ko & Jee 2018 [19]), which will be used for the rest of the analysis. While this definition of the ICL is far from perfect, and is not universal, it is a useful tool to assert whether the stacked light profiles are deep enough to make an ICL measurement, or if the measured flux is only

background variations.

The depth of the DES stacked zY images can be estimated using a method similar to that of DeMaio et al. 2015 [27] and Ko & Jee 2018 [19]: for all the 5kpc annuli between 300 and 500kpc from the center, all non-masked pixels are 3σ-clipped over 5 iterations. From the resulting sample, the standard deviation and median is taken. The flux detection threshold of the image is then the error in the weighted average of the medians, weighted by their standard deviations. For the DES images, this value is $\sim$ 2.2 counts/s, or 26.2 mag/arcsec^2. The value is coherent for these exposure times with the predicted values by DECam's Exposure Time Calculator (ETC) of 27 mag/arcsec^2 and 25.5 mag/arcsec^2 for the z and Y bands respectively. In addition, depending on the redshift bin of interest, the stacking process allow to deepen the profiles. Values of the detection threshold in various redshifts bins are presented in §4.3.1.

Now to make the comparison with the estimated value, the $\sim$ 26 mag/arcsec^2 rest-frame r-band value must be corrected to the observed zY filter used in the analysis. Using the k-correction presented in §4.2.3 and Equation 4.13, and in a similar fashion to Burke et al. 2015 [2] and Furnell et al. 2021 [4], the profile is converted from one filter to the other. The results are shown in §4.3.1.

4.2.7 Effects of the PSF on ICL measurements

A few studies (eg: Bernstein 2007 [72]) have shown that the influence of the extended PSF on surface brightness varies greatly for different ground based telescopes, and that this effect should be studied on a case-by-case basis.

In the case of DECam, the PSF of the telescope was investigated at length by Zhang et al. 2019 [11]. The study found that the extended wings of the PSF affected the flux measurement mostly in the inner 10kpc at $z = 0.25$, by decreasing the flux in the area. Beyond that, they deem the effect of the PSF negligible ($\sim 1\%$).

A back of the envelope calculation allows to compare this 10kpc at $z = 0.25$ to the redshift range presented in this study, to find that the effect of PSF affects at most the inner 22kpc flux measurements, for the highest redshifts, and at least the inner 8kpc. Since these areas are mostly associated with the central galaxy and its halo, the effect on the ICL detection at larger radii should be negligible.

4.3 Results

4.3.1 Depth of the Images

The results in the estimation of the surface brightness depth for the stacked profile are shown in Table 4.2, in the σ_{bkg} column, as a function of the redshift bin and the number of files stacked in the bin. Similarly, the results for the conversion of the SB limit from rest-frame

r-band to observed zY-band are shown in the μ_{ICL} column of Table 4.2 for each redshift bin.

The results indicate that the redshift bin $1 < z < 1.2$ is the depth limit for the cluster sample presented here; as it is the redshift bin with the most clusters, and which stands at the depth limit for the detection of the ICL. While this SB limit is neither absolute nor well defined, it still provides with a way to define the cut in depth.

Therefore, all further analysis is carried out on the reduced sample spanning $0.175 \leq z \leq 1.2$, which includes 728 clusters.

bin	# of clusters	σ_{bkg} mag/arcsec^2	μ_{ICL} mag/arcsec^2
-	1	26.2	-
$0.2 < z < 0.3$	35	28.2	26.9
$0.5 < z < 0.6$	88	28.6	27.4
$0.7 < z < 0.8$	56	28.4	27.6
$1 < z < 1.2$	218	29.1	29.1
$1.5 < z < 1.6$	28	28	31.1

Table 4.2: Flux detection limit for different redshift bins depending on the number of clusters stacked in each bin, as well as the corresponding ICL surface brightness threshold at that redshift.

4.3.2 Integrated Flux

The integrated surface brightness in 50 kpc bins is shown in Figure 4.7, for four bins: $1 \leq r < 56$, $56 \leq r < 106$, $106 \leq r < 156$, and $156 \leq r < 206$ kpc.

There are two features on the Figure that should be noted. First, there is a slight gradient

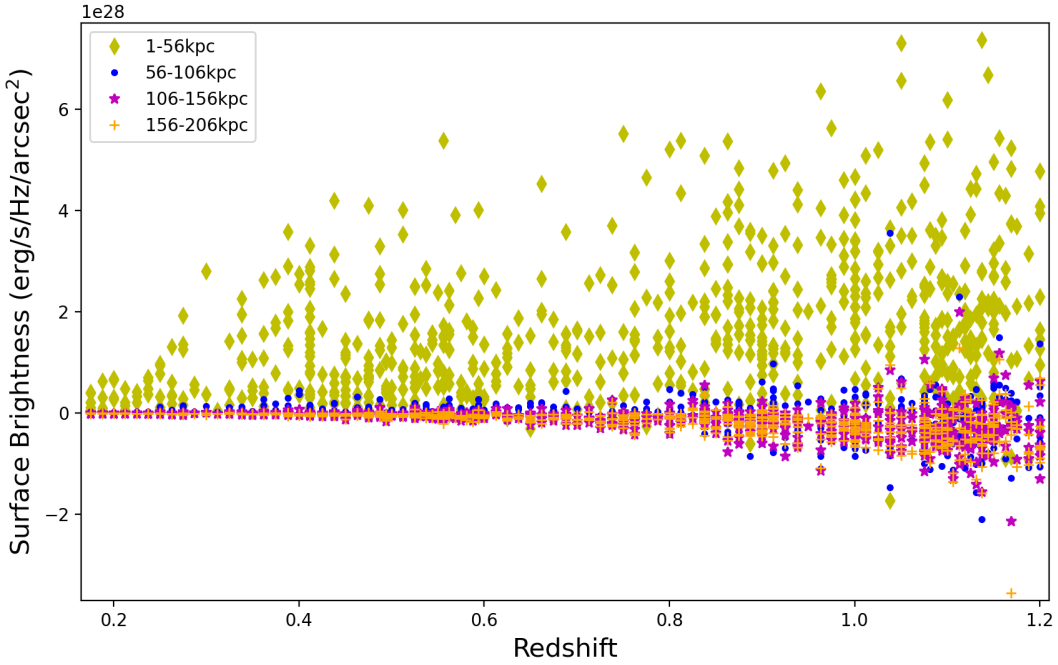

Figure 4.7: Integrated flux in 50 kpc bins for all the clusters in the $0.175 \leq z \leq 1.2$ redshift range.

in flux from the inner bins to the outer bins. The central one (green-ish diamonds), which is dominated by flux from the BCG, shows a large flux excess compared to the other three. The next bin (blue dots), which directly targets the region where the ICL should be the most concentrated, shows far lower values of detected flux - which is expected -, which are still above zero at almost all redshifts, and slightly higher than the two other bins. Then, the two outer bins (purple stars and orange crosses) are both consistent with zero.

The second interesting feature in Figure 4.7 is the complete absence of the excess flux in the $56 \leq r < 106$ kpc bin for the lowest redshifts - and the stark reduction of the flux in the

$1 \leq r < 56$ kpc bin -, up until $z \sim 0.25$. Looking back at the background subtraction by SWARP, and Figure 4.4, this is most likely due to the over-subtraction of the ICL by the software, as the size of the mesh was small enough to detect and subtract variations in the intra-cluster light.

4.3.3 Light Profiles

The resulting stacked light profiles for five redshift bins are shown in Figure 4.8, along with the converted profile from Zhang et al. 2019 [11]. The curves are the rest-frame surface brightness of the clusters out to 500 kpc from the BCG. The figure shows the curves of growth with two different correction prescriptions: the profiles in the top panel are only k-corrected, whereas the curves in the bottom panel are also corrected for evolution, i.e.: the profile has been aged to $z = 0$ assuming a single burst of star formation at $z = 3$, with solar metallicity. This redshift of formation is chosen as it is the standard redshift used in the literature, and thus allows to com[are with other studies. In a similar fashion to what can be seen in Figure 4.7, all curves show an excess flux up to $\sim$ 100kpc. However, it should be noted that as shown in §4.3.1, the highest redshift bin is not deep enough to have a reliable estimate of the ICL in the region, and that the lowest redshift been is likely over-subtracted by the image processing pipeline from Morganson et al. 2018 [10].

Moreover, the top panel clearly shows a gradient in which the highest redshift clusters are brighter than the lower redshift ones. This gradient completely disappears when correcting

for the evolution of the stellar populations, as shown in the bottom panel. In this case, the curves become strikingly similar, and are consistent with being in agreement with one another. The implications of these results for the clusters are discussed in §5.

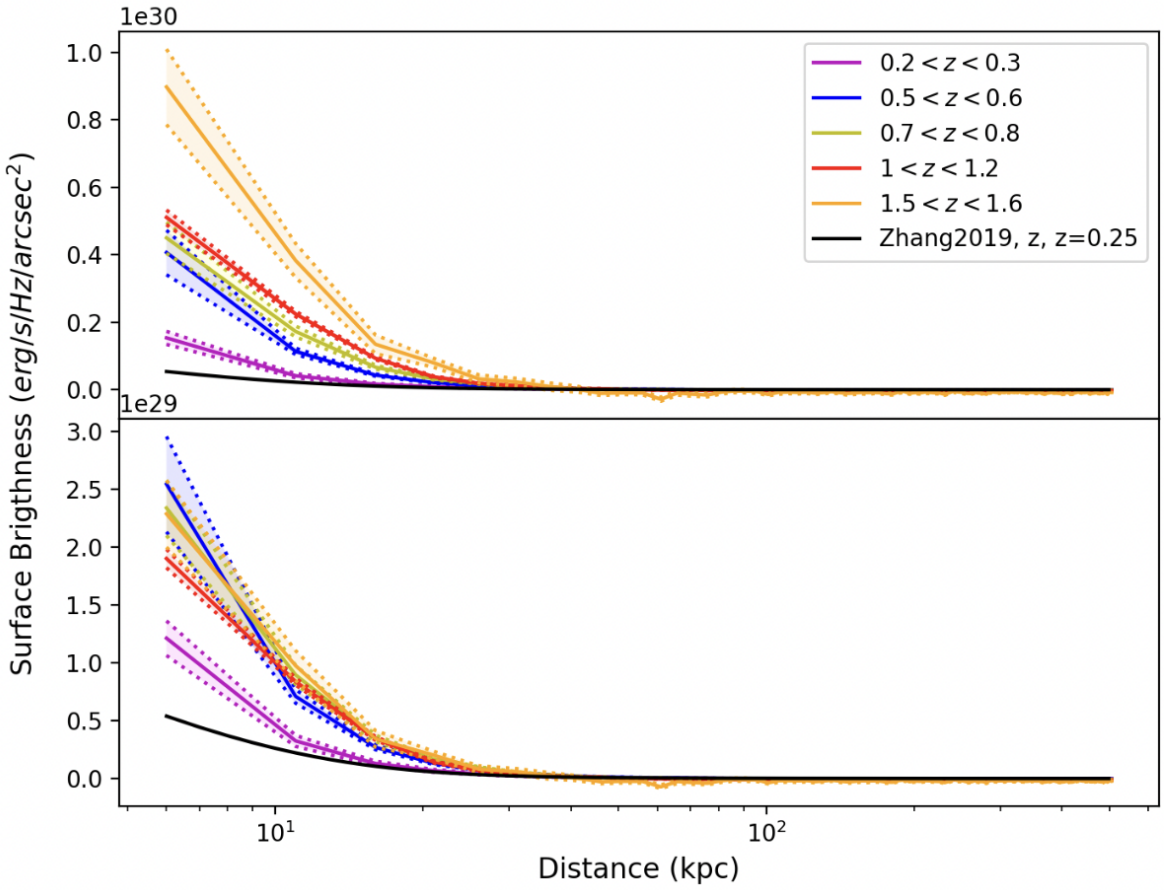

Figure 4.8: Stacked light profiles for the redshift bins. Highlighted areas are the errors in the profiles from the jackknife method. The black line is the best-fit profile from Zhang et al. 2019 [11], corrected to the observed zY-band. The top panel is only been k-corrected, whereas the bottom panel is both k- and e-corrected. Almost all the differences in amplitude between the cruves disappear with the evolution correction.

Chapter 5

Discussion

The section was written exclusively by C. Barfety.

5.1 *In-situ* Formation of the ICL in SpARCSJ1049

Using the pixel-by-pixel M/L map of the region surrounding the cluster core in SpARCSJ1049, it was possible to estimate that $(1.00 \pm 0.18) \times 10^{11}\ M_{\odot}$ of stars are sitting in the ICM, forming what looks like a tidal tail. This mass also happens to be spatially coincident with a high SFR ($\sim 860\ M_{\odot}/yr$, Webb et al. 2015b [7]) and a giant molecular gas reservoir ($\sim 10^{11}\ M_{\odot}$, Webb et al. 2017 [50], Barfety et al. in prep).

The cluster was also recently identified as a cooling flow by Hlavacek-Larrondo et al. 2020 [9], and the peak of the X-ray emission is centered on the same region as the gas reservoir and SFR. All these facts together paint the portrait of a burst of star formation,

triggered by the cooling flow, which appears to have formed the mass already detected, and will keep on forming stars using the available molecular gas. In this situation, where the central galaxy appears to have been knocked from the cluster potential, it is therefore likely that the mass formed is in fact feeding the intra-cluster light.

If the ICL stellar mass fraction is considered to be roughly $\sim 10 - 20\%$, which seems to be the average ICL fraction based on the literature, it is possible to make a crude estimate for the fraction of ICL formed in the starbursting event. The mass of the cluster halo, as measured by Webb et al. 2015b [7], is $3.8 \times 10^{14}\, M_{\odot}$; where $\sim 4 \times 10^{12}\, M_{\odot}$ is expected to be galaxies. This implies that the ICL would have a mass of $\sim 8 \times 10^{11}\, M_{\odot}$ at low redshift. If the SF formation efficiently converts the molecular gas reservoir into a new stellar population, the mass in the area would approximately double, to reach $\sim 2 \times 10^{11}\, M_{\odot}$. This event would then have formed $\sim 25\%$ of the ICL at $z = 1.71$. This can make sense if, as surmised by Rudick et al. 2006, 2009 [28, 45], the ICL forms in discrete events related to the dynamical state of the cluster (although these two studies refer to accretion events specifically).

While there has been various studies reporting *in-situ* ICL formation (Sun et al. 2010 [37], Smith et al. 2010, Gullieuszik et al. 2020 [40]), SF fed by a cooling flow has neither been observed nor brought forth as a potential source of ICL, and it particular not in these proportions. This could be - in part - because of the lack of high-resolution multi-wavelength imaging of high-redshift clusters. In the case of SpARCSJ1049, the extraordinary wealth of data is what permits the reconstruction of the cluster's evolution. It is also possible that

this cluster is an exception, where all the necessary conditions - no AGN feedback, BCG knocked out of the cluster potential - are met for this event to take place.

That being said, whether the cluster is an exception, or a new channel of formation entirely; it offers an exciting new insight on the formation of the ICL, which challenges most theories to date. Moreover, if this event does in fact form $\sim 50\%$ of the ICL, it would support the results from Jiménez-Teja et al. 2018 [30] in which the formation of the ICL is tightly linked to the dynamical state of the cluster, rather than a strict function of redshift.

5.2 Evolution of the ICL in the SpARCS clusters

Shown in Figure 4.8, the evolved stacked profiles for the three redshift bins are strikingly similar in both shape and amplitude for the (e+k)-corrected profiles; with a gradient in the non e-corrected profiles where the highest redshift curve is the brightest and the closest curve is the dimmest. This result is in stark contrast with any study of the ICL to this day, and the following sections discuss the implications and possible explanations for this.

5.2.1 Younger Stellar Populations in the ICL

The k- and e-corrections applied to the light profiles are built on simple stellar population models formed through a single burst of star formation at $z = 3$. This means the ICL stars would be ~ 11 Gyr-old. Based on the studies presented in §2.1.4, the ICL is in fact younger than that: the stars appear to be between 8.5 Gyr old (Cui et al. 2014. [34]) and 7 Gyr old

(Morishita et al. 2017 [29]) for $M_{500} \sim 10^{15}\,M_{\odot}$ clusters, which puts their epoch of formation anywhere in the range $0.8 < z < 1.3$. Ko & Jee 2018 [19] also makes an estimate for the epoch of formation of the ICL, around $z \sim 2$, for a cluster of mass $M_{500} = 3.4 \times 10^{14}\,M_{\odot}$. Even basing the age of the ICL on the results from the analysis of SpARCSJ1049 would give a formation redshift of $z = 1.7$, much lower than that assumed in the Bruzual & Charlot models.

Moreover, since a lot of studies observe color gradients in the ICL, it is very likely that a single burst of star formation is too simple a model to correctly represent its stellar population. Both of these facts imply that the evolutionary correction applied here might not be severe enough to account for the young stars in the high redshift profile, and thus explain why the high redshift profile has a surface brightness profile brighter than the lower redshift ones.

5.2.2 Dependency of the ICL on the Cluster Mass

The selection criterion of the SpARCS clusters tends to bias the sample into having cluster masses $\sim 2 \times 10^{14}\,M_{\odot}$, as mentioned in §4.1.1. This means that the clusters analysed in this work are not an evolutionary sequence, i.e. the clusters at $z = 1$ are not progenitors of those at $z = 0.175$. This has interesting consequences for the profiles displayed in Figure 4.8.

If there is no dependence on the cluster mass, then what these results imply is that there is no redshift evolution in neither the BCG nor the ICL from $z \sim 1$ to the local Universe,

which is highly unlikely, based on the results from both observations and simulations.

It is thus more probable that, as predicted by DeMaio et al. 2018 [17] and Zhang et al. 2019 [11], there is a mass dependence in the evolution of the ICL, in which case these profiles can be interpreted very differently. In this situation, the same amount of intra-cluster light is expected in the clusters, independent of redshift. The fact that the evolution correction essentially erases all the differences between the curves therefore means that the differences in amplitude might only result from the evolution of the stellar populations: the stellar population of the clusters at $z = 1$ might be younger, and thus are brighter than at $z = 0.5$. Under this train of thought, the ICL would therefore be composed of stars formed around the same epoch, seemingly between $1 < z < 2$, but assembled to form the ICL as the cluster grows in mass, rather than as a function of redshift.

5.2.3 Co-Evolution of the BCG and ICL

Another interesting feature of Figure 4.8 is the apparent co-evolution of the surface brightness in the inner 10kpc (dominated by the central galaxy), with that of the surface brightness out to 100 kpc (dominated by the ICL). This is in contradiction with studies focusing on the evolution of both components, which observe a decoupling of the BCG and ICL components, where the BCG already formed most of its mass by $z = 1$, whereas the ICL mainly grows after that time (Contini et al. 2014, 2018 [5, 21], Burke et al. 2015 [2]. Similarly, DeMaio et al. 2018 observes a very different growth rate between the light in the inner 10kpc compared

to that of the inner 100 kpc ($M \propto M_{500,c}^{0.17\pm0.06}$ vs $M \propto M_{500,c}^{0.37\pm0.05}$ respectively).

On the other hand, the results presented here imply a similar evolution of the BCG and ICL components. That also means that the discussion in the two above sections also apply for the growth of the BCG, in terms of both the cluster mass dependence and the age of the stellar populations. This is in line with the observations from Ko & Jee 2018 [19], which find ICL production to be linked to BCG formation in their $z = 1.24$ cluster.

It should be noted that the curves do present an slight difference in shape, where the lower redshift ones display a steeper increase of the light in the central region compared to the outer regions. This could be a sign of a change in the cluster's light distribution depending on redshift, however the present systematics on the profiles do not allow for a more detailed investigation and certain conclusion.

5.2.4 Comparison to Zhang et al. 2019

Plotted as the black line in Figure 4.8, the corrected profile from Zhang et al. 2019 [11] displays a much lower amplitude at $z = 0.25$ compared to the results from this analysis. A few explanations for this effect are investigated below:

- If the excess in light in the analysis came from an error in the masking of foreground and background objects, then the expected excess in light should be observed on the entire distance range. However, the curves from the SpARCS clusters and the one from Zhang et al. 2019 [11] clearly converge to the same background values out to 500 kpc.

- It is possible that the masking prescription presented here does not efficiently account for the halos of cluster galaxies, which are concentrated around the cluster center; and that it results in an increasing contamination of the measurement as the radii decreases. While this means that the absolute measurements of the surface brightness in the profiles are skewed, this effect should be the same across all profiles, as the cluster masses are in the same range, and therefore the interpretation presented above should not be affected by this.

- Finally, if, as surmised above, the ICL is younger than the evolution correction assumes here, then the curves presented in Figure 4.8 are not completely corrected, and thus the gap in evolution is not fully filled in the bottom panel.

Zhang et al. 2019 [11] also noted that their aggressive ”cleaning” of the ICL profile likely resulted in the over-subtraction of flux, and therefore that the fitted profile is expected to be an under-estimation of the ”true” ICL profile.

Chapter 6

Conclusion

This work presents the study of the ICL in SpARCS clusters at various redshifts, using two different methods. The results are as follow:

- There is $(1.00 \pm 0.18) \times 10^{11}\, M_{\odot}$ of stars recently formed in the ICM of SpARCSJ1049. Given the presence of a cool core in the cluster, this might be the first detection of a significant amount of intra-cluster stars forming *in-situ*. It would also be the highest redshift ICL detection to date, at $z = 1.71$.

- The analysis of the light profiles from the SpARCS clusters between $0.5 < z < 1.2$ points toward a strong dependence in the BCG+ICL light with cluster mass, rather than redshift. Moreover, the results of the evolution correction suggest that the stars form at the same epoch, but assemble to form the ICL at different times depending on the cluster mass.

- It is likely that the stars in the ICL form at later times compared to the usual prescription used in stellar population models of $z = 3$, and might also form in multiple bursts of SF, which would explain the colour gradients.

- It is possible that the masking algorithm presented in this work does not sufficiently account for the halos of cluster galaxies, which leads to an overestimation of the surface brightness in the inner regions of the cluster.

6.1 Future Work

Going forward, it would be interesting to investigate cluster samples which vary in either mass or redshift, but not both, to better quantify the dependence of the BCG + ICL light on both variables. Investigating the age of the ICL stars in local clusters spanning a wide mass range would also help confirm or infirm the possibilities discussed here. On the other hand, focusing the cluster selection on the dynamical state of clusters, as did Jiménez-Teja et al. 2018 [30], rather than their absolute mass or redshift, could be a novel way to investigate the intra-cluster light.

As shown in this thesis, as well as in Zhang et al. 2019 [11] and Sampaio-Santos et al. 2021 [31], stacking offers exciting new prospects for the investigation of the ICL at higher redshifts, or with shallower data. Moreover, new facilities, such as the James Webb Space Telescope (JWST), will allow for deeper imaging of high redshift clusters, with resolution even better

than that of HST. Lastly, multi-wavelength analysis of clusters at distinct redshifts/masses, such as the one realized on SpARCSJ1049, present an interesting alternative in studying the ICL: finding how the ICL fits in in the picture of the cluster's state could help understand its formation mechanisms in more depth.

Finally, it appears imperative that studies define and investigate the ICL in more uniform ways: comparison between both observational and theoretical works have been complicated by the differences in ICL definitions; and it has been shown that different characterizations lead to starkly different results (Tang et al. 2018 [6]). It has been proposed that theoretical studies should define the intra-cluster light in the same way as the observational ones, to see if some of the tension between the two can be resolved (Furnell et al. 2021 [4]). This would also allow for interesting comparisons on how the ICL fraction varies within simulations using the SBL method compared to the fraction extracted directly since its formation.

It should be noted that there are several caveats in the analysis that will be addressed in the future: the effect of the background subtraction by SEXTRACTOR will be investigated in more detail, and if necessary, cuts will be made to redshift ranges that are too strongly affected. In addition, it has been observed that the Y filter brings a lot of additional noise in the images, and the work will therefore continue focusing on the z-band images.

Bibliography

[1] C. S. Rudick, J. C. Mihos, and C. K. McBride, "The Quantity of Intracluster Light: Comparing Theoretical and Observational Measurement Techniques using Simulated Clusters," *ApJ*, vol. 732, p. 48, May 2011.

[2] C. Burke, M. Hilton, and C. Collins, "Coevolution of brightest cluster galaxies and intracluster light using CLASH," *MNRAS*, vol. 449, pp. 2353–2367, May 2015.

[3] M. Montes and I. Trujillo, "Intracluster light at the Frontier - II. The Frontier Fields Clusters," *MNRAS*, vol. 474, pp. 917–932, Feb. 2018.

[4] K. E. Furnell, C. A. Collins, L. S. Kelvin, I. K. Baldry, P. A. James, M. Manolopoulou, R. G. Mann, P. A. Giles, A. Bermeo, M. Hilton, R. Wilkinson, A. K. Romer, C. Vergara, S. Bhargava, J. P. Stott, J. Mayers, and P. Viana, "The growth of intracluster light in XCS-HSC galaxy clusters from 0.1 ¡ z ¡ 0.5," *MNRAS*, vol. 502, pp. 2419–2437, Apr. 2021.

[5] E. Contini, G. De Lucia, Á. Villalobos, and S. Borgani, "On the formation and physical properties of the intracluster light in hierarchical galaxy formation models," *MNRAS*, vol. 437, pp. 3787–3802, Feb. 2014.

[6] L. Tang, W. Lin, W. Cui, X. Kang, Y. Wang, E. Contini, and Y. Yu, "An Investigation of Intracluster Light Evolution Using Cosmological Hydrodynamical Simulations," *ApJ*, vol. 859, p. 85, June 2018.

[7] T. Webb, A. Noble, A. DeGroot, G. Wilson, A. Muzzin, N. Bonaventura, M. Cooper, A. Delahaye, R. Foltz, C. Lidman, J. Surace, H. K. C. Yee, S. Chapman, L. Dunne, J. Geach, B. Hayden, H. Hildebrandt, J. Huang, A. Pope, M. W. L. Smith, S. Perlmutter, and A. Tudorica, "An Extreme Starburst in the Core of a Rich Galaxy Cluster at z = 1.7," *ApJ*, vol. 809, p. 173, Aug. 2015.

[8] K. Finner, M. James Jee, T. Webb, G. Wilson, S. Perlmutter, A. Muzzin, and J. Hlavacek-Larrondo, "Constraining the Mass of the Emerging Galaxy Cluster SpARCS1049+56 at z = 1.71 with Infrared Weak Lensing," *ApJ*, vol. 893, p. 10, Apr. 2020.

[9] J. Hlavacek-Larrondo, C. L. Rhea, T. Webb, M. McDonald, A. Muzzin, G. Wilson, K. Finner, F. Valin, N. Bonaventura, M. Cooper, A. C. Fabian, M. L. Gendron-Marsolais, M. J. Jee, C. Lidman, M. Mezcua, A. Noble, H. R. Russell, J. Surace, A. Trudeau, and H. K. C. Yee, "Evidence of Runaway Gas Cooling in the Absence of

Supermassive Black Hole Feedback at the Epoch of Cluster Formation," *ApJL*, vol. 898, p. L50, Aug. 2020.

[10] E. Morganson, R. A. Gruendl, F. Menanteau, M. Carrasco Kind, Y. C. Chen, G. Daues, A. Drlica-Wagner, D. N. Friedel, M. Gower, M. W. G. Johnson, M. D. Johnson, R. Kessler, F. Paz-Chinchón, D. Petravick, C. Pond, B. Yanny, S. Allam, R. Armstrong, W. Barkhouse, K. Bechtol, A. Benoit-Lévy, G. M. Bernstein, E. Bertin, E. Buckley-Geer, R. Covarrubias, S. Desai, H. T. Diehl, D. A. Goldstein, D. Gruen, T. S. Li, H. Lin, J. Marriner, J. J. Mohr, E. Neilsen, C. C. Ngeow, K. Paech, E. S. Rykoff, M. Sako, I. Sevilla-Noarbe, E. Sheldon, F. Sobreira, D. L. Tucker, W. Wester, and DES Collaboration, "The Dark Energy Survey Image Processing Pipeline," *PASP*, vol. 130, p. 074501, July 2018.

[11] Y. Zhang, B. Yanny, A. Palmese, D. Gruen, C. To, E. S. Rykoff, Y. Leung, C. Collins, M. Hilton, T. M. C. Abbott, J. Annis, S. Avila, E. Bertin, D. Brooks, D. L. Burke, A. Carnero Rosell, M. Carrasco Kind, J. Carretero, C. E. Cunha, C. B. D'Andrea, L. N. da Costa, J. De Vicente, S. Desai, H. T. Diehl, J. P. Dietrich, P. Doel, A. Drlica-Wagner, T. F. Eifler, A. E. Evrard, B. Flaugher, P. Fosalba, J. Frieman, J. García-Bellido, E. Gaztanaga, D. W. Gerdes, R. A. Gruendl, J. Gschwend, G. Gutierrez, W. G. Hartley, D. L. Hollowood, K. Honscheid, B. Hoyle, D. J. James, T. Jeltema, K. Kuehn, N. Kuropatkin, T. S. Li, M. Lima, M. A. G. Maia, M. March, J. L. Marshall, P. Melchior, F. Menanteau, C. J. Miller, R. Miquel, J. J. Mohr, R. L. C. Ogando, A. A. Plazas, A. K.

Romer, E. Sanchez, V. Scarpine, M. Schubnell, S. Serrano, I. Sevilla-Noarbe, M. Smith, M. Soares-Santos, F. Sobreira, E. Suchyta, M. E. C. Swanson, G. Tarle, D. Thomas, W. Wester, and DES Collaboration, "Dark Energy Survey Year 1 Results: Detection of Intracluster Light at Redshift ˜ 0.25," *ApJ*, vol. 874, p. 165, Apr. 2019.

[12] A. Oemler, "The cluster of galaxies Abell 2670.," *ApJ*, vol. 180, pp. 11–23, Apr. 1973.

[13] F. Zwicky, "On the Masses of Nebulae and of Clusters of Nebulae," *ApJ*, vol. 86, p. 217, Oct. 1937.

[14] F. Zwicky, "The Coma Cluster of Galaxies," *PASP*, vol. 63, p. 61, Apr. 1951.

[15] J. Oemler, A., "The structure of elliptical and cD galaxies.," *ApJ*, vol. 209, pp. 693–709, Nov. 1976.

[16] R. Vilchez-Gomez, R. Pello, and B. Sanahuja, "Detection of intracluster light in the rich clusters of galaxies Abell 2390 and CL 1613+31.," *AAP*, vol. 283, pp. 37–50, Mar. 1994.

[17] T. DeMaio, A. H. Gonzalez, A. Zabludoff, D. Zaritsky, T. Connor, M. Donahue, and J. S. Mulchaey, "Lost but not forgotten: intracluster light in galaxy groups and clusters," *MNRAS*, vol. 474, pp. 3009–3031, Mar. 2018.

[18] T. DeMaio, A. H. Gonzalez, A. Zabludoff, D. Zaritsky, G. Aldering, M. Brodwin, T. Connor, M. Donahue, B. Hayden, J. S. Mulchaey, S. Perlmutter, and S. A. Stanford,

"The growth of brightest cluster galaxies and intracluster light over the past 10 billion years," *MNRAS*, vol. 491, pp. 3751–3759, Jan. 2020.

[19] J. Ko and M. J. Jee, "Evidence for the Existence of Abundant Intracluster Light at z = 1.24," *ApJ*, vol. 862, p. 95, Aug. 2018.

[20] C. Burke, C. A. Collins, J. P. Stott, and M. Hilton, "Measurement of the intracluster light at z $\sim$ 1," *MNRAS*, vol. 425, pp. 2058–2068, Sept. 2012.

[21] E. Contini, S. K. Yi, and X. Kang, "The different growth pathways of brightest cluster galaxies and intracluster light," *MNRAS*, vol. 479, pp. 932–944, Sept. 2018.

[22] E. Puchwein, V. Springel, D. Sijacki, and K. Dolag, "Intracluster stars in simulations with active galactic nucleus feedback," *MNRAS*, vol. 406, pp. 936–951, Aug. 2010.

[23] E. F. Bell, D. H. McIntosh, N. Katz, and M. D. Weinberg, "The Optical and Near-Infrared Properties of Galaxies. I. Luminosity and Stellar Mass Functions," *ApJs*, vol. 149, pp. 289–312, Dec. 2003.

[24] M. Montes, "The intracluster light and its role in galaxy evolution in clusters," *arXiv e-prints*, p. arXiv:1912.01616, Dec. 2019.

[25] J. J. Feldmeier, J. C. Mihos, H. L. Morrison, P. Harding, N. Kaib, and J. Dubinski, "Deep CCD Surface Photometry of Galaxy Clusters. II. Searching for Intracluster Starlight in Non-cD clusters," *ApJ*, vol. 609, pp. 617–637, July 2004.

[26] A. H. Gonzalez, D. Zaritsky, and A. I. Zabludoff, "A Census of Baryons in Galaxy Clusters and Groups," *ApJ*, vol. 666, pp. 147–155, Sept. 2007.

[27] T. DeMaio, A. H. Gonzalez, A. Zabludoff, D. Zaritsky, and M. Bradač, "On the origin of the intracluster light in massive galaxy clusters," *MNRAS*, vol. 448, pp. 1162–1177, Apr. 2015.

[28] C. S. Rudick, J. C. Mihos, and C. McBride, "The Formation and Evolution of Intracluster Light," *ApJ*, vol. 648, pp. 936–946, Sept. 2006.

[29] T. Morishita, L. E. Abramson, T. Treu, K. B. Schmidt, B. Vulcani, and X. Wang, "Characterizing Intracluster Light in the Hubble Frontier Fields," *ApJ*, vol. 846, p. 139, Sept. 2017.

[30] Y. Jiménez-Teja, R. Dupke, N. Benítez, A. M. Koekemoer, A. Zitrin, K. Umetsu, B. L. Ziegler, B. L. Frye, H. Ford, R. J. Bouwens, L. D. Bradley, T. Broadhurst, D. Coe, M. Donahue, G. J. Graves, C. Grillo, L. Infante, S. Jouvel, D. D. Kelson, O. Lahav, R. Lazkoz, D. Lemze, D. Maoz, E. Medezinski, P. Melchior, M. Meneghetti, A. Mercurio, J. Merten, A. Molino, L. A. Moustakas, M. Nonino, S. Ogaz, A. G. Riess, P. Rosati, J. Sayers, S. Seitz, and W. Zheng, "Unveiling the Dynamical State of Massive Clusters through the ICL Fraction," *ApJ*, vol. 857, p. 79, Apr. 2018.

[31] H. Sampaio-Santos, Y. Zhang, R. L. C. Ogando, T. Shin, J. B. Golden-Marx, B. Yanny, K. Herner, M. Hilton, A. Choi, M. Gatti, D. Gruen, B. Hoyle, M. M. Rau, J. De

Vicente, J. Zuntz, T. M. C. Abbott, M. Aguena, S. Allam, J. Annis, S. Avila, E. Bertin, D. Brooks, D. L. Burke, M. Carrasco Kind, J. Carretero, C. Chang, M. Costanzi, L. N. da Costa, H. T. Diehl, P. Doel, S. Everett, A. E. Evrard, B. Flaugher, P. Fosalba, J. Frieman, J. García-Bellido, E. Gaztanaga, D. W. Gerdes, R. A. Gruendl, J. Gschwend, G. Gutierrez, S. R. Hinton, D. L. Hollowood, K. Honscheid, D. J. James, M. Jarvis, T. Jeltema, K. Kuehn, N. Kuropatkin, O. Lahav, M. A. G. Maia, M. March, J. L. Marshall, R. Miquel, A. Palmese, F. Paz-Chinchón, A. A. Plazas, E. Sanchez, B. Santiago, V. Scarpine, M. Schubnell, M. Smith, E. Suchyta, G. Tarle, D. L. Tucker, T. N. Varga, and R. H. Wechsler, "Is diffuse intracluster light a good tracer of the galaxy cluster matter distribution?," *MNRAS*, vol. 501, pp. 1300–1315, Feb. 2021.

[32] G. Murante, M. Giovalli, O. Gerhard, M. Arnaboldi, S. Borgani, and K. Dolag, "The importance of mergers for the origin of intracluster stars in cosmological simulations of galaxy clusters," *MNRAS*, vol. 377, pp. 2–16, May 2007.

[33] C. W. Purcell, J. S. Bullock, and A. R. Zentner, "Shredded Galaxies as the Source of Diffuse Intrahalo Light on Varying Scales," *ApJ*, vol. 666, pp. 20–33, Sept. 2007.

[34] W. Cui, G. Murante, P. Monaco, S. Borgani, G. L. Granato, M. Killedar, G. De Lucia, V. Presotto, and K. Dolag, "Characterizing diffused stellar light in simulated galaxy clusters," *MNRAS*, vol. 437, pp. 816–830, Jan. 2014.

[35] S. Schulz and C. Struck, "Multi stage three-dimensional sweeping and annealing of disc galaxies in clusters," *MNRAS*, vol. 328, pp. 185–202, Nov. 2001.

[36] B. Vollmer, V. Cayatte, C. Balkowski, and W. J. Duschl, "Ram Pressure Stripping and Galaxy Orbits: The Case of the Virgo Cluster," *ApJ*, vol. 561, pp. 708–726, Nov. 2001.

[37] M. Sun, M. Donahue, E. Roediger, P. E. J. Nulsen, G. M. Voit, C. Sarazin, W. Forman, and C. Jones, "Spectacular X-ray Tails, Intracluster Star Formation, and ULXs in A3627," *ApJ*, vol. 708, pp. 946–964, Jan. 2010.

[38] B. R. McNamara and P. E. J. Nulsen, "Mechanical feedback from active galactic nuclei in galaxies, groups and clusters," *New Journal of Physics*, vol. 14, p. 055023, May 2012.

[39] R. J. Smith, J. R. Lucey, D. Hammer, A. E. Hornschemeier, D. Carter, M. J. Hudson, R. O. Marzke, M. Mouhcine, S. Eftekharzadeh, P. James, H. Khosroshahi, E. Kourkchi, and A. Karick, "Ultraviolet tails and trails in cluster galaxies: a sample of candidate gaseous stripping events in Coma," *MNRAS*, vol. 408, pp. 1417–1432, Nov. 2010.

[40] M. Gullieuszik, B. M. Poggianti, S. L. McGee, A. Moretti, B. Vulcani, S. Tonnesen, E. Roediger, Y. L. Jaffé, J. Fritz, A. Franchetto, A. Omizzolo, D. Bettoni, M. Radovich, and A. Wolter, "GASP. XXI. Star Formation Rates in the Tails of Galaxies Undergoing Ram Pressure Stripping," *ApJ*, vol. 899, p. 13, Aug. 2020.

[41] J. Melnick, E. Giraud, I. Toledo, F. Selman, and H. Quintana, "Intergalactic stellar populations in intermediate redshift clusters," *MNRAS*, vol. 427, pp. 850–858, Nov. 2012.

[42] C. Conroy, R. H. Wechsler, and A. V. Kravtsov, "The Hierarchical Build-Up of Massive Galaxies and the Intracluster Light since z = 1," *ApJ*, vol. 668, pp. 826–838, Oct. 2007.

[43] C. L. Mancone, T. Baker, A. H. Gonzalez, M. L. N. Ashby, S. A. Stanford, M. Brodwin, P. R. M. Eisenhardt, G. Snyder, D. Stern, and E. L. Wright, "The Faint End of the Cluster-galaxy Luminosity Function at High Redshift," *ApJ*, vol. 761, p. 141, Dec. 2012.

[44] J. C. Mihos, "Interactions and Mergers of Cluster Galaxies," in *Clusters of Galaxies: Probes of Cosmological Structure and Galaxy Evolution* (J. S. Mulchaey, A. Dressler, and A. Oemler, eds.), p. 277, Jan. 2004.

[45] C. S. Rudick, J. C. Mihos, L. H. Frey, and C. K. McBride, "Tidal Streams of Intracluster Light," *ApJ*, vol. 699, pp. 1518–1529, July 2009.

[46] G. Wilson, A. Muzzin, H. K. C. Yee, M. Lacy, J. Surace, D. Gilbank, K. Blindert, H. Hoekstra, S. Majumdar, R. Demarco, J. P. Gardner, M. D. Gladders, and C. Lonsdale, "Spectroscopic Confirmation of a Massive Red-Sequence-Selected Galaxy Cluster at z = 1.34 in the SpARCS-South Cluster Survey," *ApJ*, vol. 698, pp. 1943–1950, June 2009.

[47] A. Muzzin, G. Wilson, H. K. C. Yee, H. Hoekstra, D. Gilbank, J. Surace, M. Lacy, K. Blindert, S. Majumdar, R. Demarco, J. P. Gardner, M. Gladders, and C. Lonsdale, "Spectroscopic Confirmation of Two Massive Red-Sequence-Selected Galaxy Clusters at z ~1.2 in the SpARCS-North Cluster Survey," *ApJ*, vol. 698, pp. 1934–1942, June 2009.

[48] R. Demarco, G. Wilson, A. Muzzin, M. Lacy, J. Surace, H. K. C. Yee, H. Hoekstra, K. Blindert, and D. Gilbank, "Spectroscopic Confirmation of Three Red-sequence Selected Galaxy Clusters at z = 0.87, 1.16, and 1.21 from the SpARCS Survey," *ApJ*, vol. 711, pp. 1185–1197, Mar. 2010.

[49] T. M. A. Webb, A. Muzzin, A. Noble, N. Bonaventura, J. Geach, Y. Hezaveh, C. Lidman, G. Wilson, H. K. C. Yee, J. Surace, and D. Shupe, "The Star Formation History of BCGs to z = 1.8 from the SpARCS/SWIRE Survey: Evidence for Significant In Situ Star Formation at High Redshift," *ApJ*, vol. 814, p. 96, Dec. 2015.

[50] T. M. A. Webb, J. Lowenthal, M. Yun, A. G. Noble, A. Muzzin, G. Wilson, H. K. C. Yee, R. Cybulski, I. Aretxaga, and D. H. Hughes, "Detection of a Substantial Molecular Gas Reservoir in a Brightest Cluster Galaxy at z = 1.7," *ApJL*, vol. 844, p. L17, Aug. 2017.

[51] H. V. Shipley, D. Lange-Vagle, D. Marchesini, G. B. Brammer, L. Ferrarese, M. Stefanon, E. Kado-Fong, K. E. Whitaker, P. A. Oesch, A. D. Feinstein, I. Labbé, B. Lundgren, N. Martis, A. Muzzin, K. Nedkova, R. Skelton, and A. van der Wel,

"HFF-DeepSpace Photometric Catalogs of the 12 Hubble Frontier Fields, Clusters, and Parallels: Photometry, Photometric Redshifts, and Stellar Masses," *ApJs*, vol. 235, p. 14, Mar. 2018.

[52] M. R. Blanton and S. Roweis, "K-Corrections and Filter Transformations in the Ultraviolet, Optical, and Near-Infrared," *AJ*, vol. 133, pp. 734–754, Feb. 2007.

[53] G. D. Coleman, C. C. Wu, and D. W. Weedman, "Colors and magnitudes predicted for high redshift galaxies.," *ApJs*, vol. 43, pp. 393–416, July 1980.

[54] A. L. Kinney, D. Calzetti, R. C. Bohlin, K. McQuade, T. Storchi-Bergmann, and H. R. Schmitt, "Template Ultraviolet to Near-Infrared Spectra of Star-forming Galaxies and Their Application to K-Corrections," *ApJ*, vol. 467, p. 38, Aug. 1996.

[55] A. Grazian, A. Fontana, C. de Santis, M. Nonino, S. Salimbeni, E. Giallongo, S. Cristiani, S. Gallozzi, and E. Vanzella, "The GOODS-MUSIC sample: a multicolour catalog of near-IR selected galaxies in the GOODS-South field," *AAP*, vol. 449, pp. 951–968, Apr. 2006.

[56] S. Andreon and P. Congdon, "The insignificant evolution of the richness-mass relation of galaxy clusters," *AAP*, vol. 568, p. A23, Aug. 2014.

[57] T. M. C. Abbott, M. Adamow, M. Aguena, S. Allam, A. Amon, S. Avila, D. Bacon, M. Banerji, K. Bechtol, M. R. Becker, G. M. Bernstein, E. Bertin, S. Bhargava, S. L.

Bridle, D. Brooks, D. L. Burke, A. Carnero Rosell, M. Carrasco Kind, J. Carretero, F. J. Castander, R. Cawthon, C. Chang, A. Choi, C. Conselice, M. Costanzi, M. Crocce, L. N. da Costa, T. M. Davis, J. De Vicente, J. DeRose, S. Desai, H. T. Diehl, J. P. Dietrich, A. Drlica-Wagner, K. Eckert, J. Elvin-Poole, S. Everett, A. E. Evrard, I. Ferrero, A. Ferté, B. Flaugher, P. Fosalba, D. Friedel, J. Frieman, J. García-Bellido, L. Gelman, D. W. Gerdes, T. Giannantonio, M. Gill, D. Gruen, R. A. Gruendl, J. Gschwend, G. Gutierrez, W. G. Hartley, S. R. Hinton, D. L. Hollowood, D. Huterer, D. J. James, T. Jeltema, M. D. Johnson, S. Kent, R. Kron, K. Kuehn, N. Kuropatkin, O. Lahav, T. S. Li, C. Lidman, H. Lin, N. MacCrann, M. A. G. Maia, T. Manning, M. March, J. L. Marshall, P. Martini, P. Melchior, F. Menanteau, R. Miquel, R. Morgan, J. Myles, E. Neilsen, R. L. C. Ogando, A. Palmese, F. Paz-Chinchón, D. Petravick, A. Pieres, A. A. Plazas, C. Pond, M. Rodriguez-Monroy, A. K. Romer, A. Roodman, E. S. Rykoff, M. Sako, E. Sanchez, B. Santiago, S. Serrano, I. Sevilla-Noarbe, J. Allyn. Smith, M. Smith, M. Soares-Santos, E. Suchyta, M. E. C. Swanson, G. Tarle, D. Thomas, C. To, P. E. Tremblay, M. A. Troxel, D. L. Tucker, D. J. Turner, T. N. Varga, A. R. Walker, R. H. Wechsler, J. Weller, W. Wester, R. D. Wilkinson, B. Yanny, Y. Zhang, R. Nikutta, M. Fitzpatrick, A. Jacques, A. Scott, K. Olsen, L. Huang, D. Herrera, S. Juneau, D. Nidever, B. A. Weaver, C. Adean, V. Correia, M. de Freitas, F. N. Freitas, C. Singulani, and G. Vila-Verde, "The Dark Energy Survey Data Release 2," *arXiv e-prints*, p. arXiv:2101.05765, Jan. 2021.

[58] G. M. Bernstein, T. M. C. Abbott, S. Desai, D. Gruen, R. A. Gruendl, M. D. Johnson, H. Lin, F. Menanteau, E. Morganson, E. Neilsen, K. Paech, A. R. Walker, W. Wester, B. Yanny, and DES Collaboration, "Instrumental response model and detrending for the Dark Energy Camera," *PASP*, vol. 129, p. 114502, Nov. 2017.

[59] E. Bertin, "SWarp: Resampling and Co-adding FITS Images Together," Oct. 2010.

[60] E. Bertin and S. Arnouts, "SExtractor: Software for source extraction.," *AAPS*, vol. 117, pp. 393–404, June 1996.

[61] R. G. Kron, "Photometry of a complete sample of faint galaxies.," *ApJs*, vol. 43, pp. 305–325, June 1980.

[62] J. B. Oke and J. E. Gunn, "Secondary standard stars for absolute spectrophotometry.," *ApJ*, vol. 266, pp. 713–717, Mar. 1983.

[63] J. B. Oke and A. Sandage, "Energy Distributions, K Corrections, and the Stebbins-Whitford Effect for Giant Elliptical Galaxies," *ApJ*, vol. 154, p. 21, Oct. 1968.

[64] G. Bruzual and S. Charlot, "Stellar population synthesis at the resolution of 2003," *MNRAS*, vol. 344, pp. 1000–1028, Oct. 2003.

[65] G. Chabrier, "Galactic Stellar and Substellar Initial Mass Function," *PASP*, vol. 115, pp. 763–795, July 2003.

[66] B. Efron, *The Jackknife, the Bootstrap and other resampling plans*. 1982.

[67] M. L. Humason, N. U. Mayall, and A. R. Sandage, "Redshifts and magnitudes of extragalactic nebulae.," *AJ*, vol. 61, pp. 97–162, Jan. 1956.

[68] D. W. Hogg, M. R. Blanton, D. J. Eisenstein, J. E. Gunn, D. J. Schlegel, I. Zehavi, N. A. Bahcall, J. Brinkmann, I. Csabai, D. P. Schneider, D. H. Weinberg, and D. G. York, "The Overdensities of Galaxy Environments as a Function of Luminosity and Color," *ApJL*, vol. 585, pp. L5–L9, Mar. 2003.

[69] D. W. Hogg, "Distance measures in cosmology," *arXiv e-prints*, pp. astro–ph/9905116, May 1999.

[70] J. L. Sérsic, "Influence of the atmospheric and instrumental dispersion on the brightness distribution in a galaxy," *Boletin de la Asociacion Argentina de Astronomia La Plata Argentina*, vol. 6, pp. 41–43, Feb. 1963.

[71] J. E. Krick and R. A. Bernstein, "Diffuse Optical Light in Galaxy Clusters. II. Correlations with Cluster Properties," *AJ*, vol. 134, pp. 466–493, Aug. 2007.

[72] R. A. Bernstein, "The Optical Extragalactic Background Light: Revisions and Further Comments," *ApJ*, vol. 666, pp. 663–673, Sept. 2007.